Schweizerische Eidgenossenschaft
Confédération suisse
Confederazione Svizzera
Confederaziun svizra

Eidgenössisches Departement für_Umwelt, Verkehr, Energie und Kommunikation UVEK

Bundesamt für Energie BFE

Final Report 31. August 2012

Layered Thermoelectric Converter (LTEC)

Auftraggeber:
Bundesamt für Energie BFE
Forschungsprogramm Elektrizitätstechnologien & -anwendungen
CH-3003 Bern
www.bfe.admin.ch

Auftragnehmer:
Empa
Department of Solid State Chemistry and Catalysis
Überlandstrasse 129
CH-8600 Dübendorf
www.empa.ch

Autoren:
Dimas Surya Alfaruq, Empa, dimas.alfaruq@empa.ch
Anke Weidenkaff, Empa, anke.weidenkaff@empa.ch

BFE-Bereichsleiter: Dr. Michael Moser
BFE-Programmleiter: Roland Brüniger
BFE-Vertrags-Nr: SI/500109-01

Table of Contents

Zusammenfassung

$CaMnO_3$ wurde in Form von polykristallinem Material, Filmen und Einkristallen hergestellt. Für die Synthese der Materialien wurde eine sogenannte „Soft Chemistry“-Methode verwendet. Zusätzlich wurde $CaMnO_3$ mit kleinen Mengen Wolfram (1%, 3%, 5%) dotiert. Von allen hergestellten Verbindungen hatte $CaMn_{0.97}W_{0.03}O_{3-\delta}$ den höchsten ZT-Wert und elektrischer Widerstand und Wärmeleitfähigkeit wurden erheblich verringert. Diese Ergebnisse sind darauf zurückzuführen, dass W eine höhere Anzahl an Elektronen in die $CaMnO_3$-Struktur einbringt und somit eine effektivere Phononenstreuung bewirkt. Unsere Untersuchungen ergaben, dass die thermoelektrischen Eigenschaften der $CaMnO_3$-Dünnfilme stark vom Syntheseweg abhängen. Mit Syntheseweg A wurden reinphasige $CaMnO_3$-Dünnfilme mit höherer Ausgangsleistung und höherem elektrischem Widerstand erhalten als mit Syntheseweg B. Ein $CaMn_{0.98}Nb_{0.02}O_{3-\delta}$ Einkristall wurde erfolgreich unter Anwendung der „Travelling Solvent Floating Zone“ (TSFZ)-Technik erzeugt. Bei der Untersuchung des Kristalles wurde eine reinphasige Region in der Kristallmitte identifiziert. Da der $CaMn_{0.98}Nb_{0.02}O_{3-\delta}$-Einkristall nahezu keine Korngrenzen besitzt, ist seine Wärmeleitfähigkeit verglichen mit polykristallinem $CaMn_{0.98}Nb_{0.02}O_{3-\delta}$ bei einer Temperatur von 300 K höher.

Abstract

$CaMnO_3$ was prepared in the form of polycrystalline material, films and single crystals. A soft chemistry method was chosen for the synthesis of the materials. In addition, $CaMnO_3$ was substituted with small amounts of tungsten (1%, 3%, 5%). Of all the prepared compounds, $CaMn_{0.97}W_{0.03}O_{3-\delta}$ had the highest ZT value and electrical resistivity, and the thermal conductivity was significantly reduced. This is due to the fact that W introduces more electrons into the $CaMnO_3$ system and scatters phonons more efficiently. The thermoelectric properties of CaMnO3 thin films were found to depend strongly on the synthesis route. Route A yielded single-phase $CaMnO_3$ thin films with higher output power and electrical resistivity than route B. A $CaMn_{0.98}Nb_{0.02}O_{3-\delta}$ single crystal was successfully grown using the Travelling Solvent Floating Zone (TSFZ) technique. The characterization of the crystal revealed a single phase region in the center of the crystal. Due to the absence of grain boundaries, the thermal conductivity of the single crystal is higher compared to the polycrystalline sample at 300 K.

1. Starting Situation

Perovskite-type oxides appear to be promising candidates among other thermoelectric materials (i.e. half-Heusler compounds [1], skutterudites [2] _ENREF_5, bismuth tellurides _ENREF_6[3]). They are chemically stable at high temperatures and thus have a high energy harvesting potential from waste heat [4]. Due to their very flexible ABO_3 crystal structure, charge carrier concentration and band structures can be modified by anionic and cationic substitution [5-7]. This allows the physical-chemical properties of the materials (i.e. the Seebeck coefficient and electrical resistivity) to be controlled.

Perovskite-type manganate phases have been widely studied by many researchers due to their interesting physical properties such as colossal magnetoresistance (CMR) [8, 9]. CMR could be explained by the competition between different magnetic interactions and charge and/or orbital ordering [10]. In particular, un-substituted $CaMnO_3$ appears to be a good n-type TE material owing to its large absolute Seebeck coefficient, which is one of the prerequisites for a potential thermoelectric (TE) material [11, 12].

Low level anionic substitution in $CaMnO_3$ is a method to induce CMR and to improve the thermoelectric properties [10,13,14]. The substitution generates Mn^{3+} ions in Mn^{4+} sites corresponding to electron doping in the e_g bands which lowers the electrical resistivity of the compounds [15, 16].

We started the project by utilizing 2% Nb substitution in $CaMnO_3$ as the basis of our research. From there, we improved the properties by synthesizing polycrystalline materials with different substitution element, thin films, and single crystal of $CaMnO_3$, respectively. Conclusively we compared their properties with 2% Nb substitution in $CaMnO_3$.

2. Project Aim

The goal of this project was to investigate and improve the thermoelectric properties of the n-type perovskite $CaMnO_3$.

3. Materials and Methods

3.1 Synthesis of $CaMnO_3$ thin films

Perovskite-type $CaMnO_3$ films were prepared by a soft chemistry method based on mixed acetate precursor solutions [17]. A 0.5 M solution was prepared by dissolving stoichiometric amounts of calcium acetate ($Ca(CH_3COO)_2.H_2O$) (Alfa Aesar, Ward Hill, MA) and manganese acetate tetrahydrate ($Mn(CH_3COO)_2.4H_2O$) (Merck, Frankfurt, Germany) were in 50 mL glacial acetic acid at 90 °C. The solution was heated at 110 °C for 10 min to partially evaporate the water of crystallization of the Ca and Mn compound and then cooled down to 50 °C. In the next step, 1.55 mL of ethylene glycol (Merck) was added with constant stirring and the solution was kept at ≈ 40 °C to avoid precipitation of the precursors.

Prior to deposition, round sapphire substrates (Stettler Sapphire AG) (1 mm thickness, 20 mm diameter, Stettler Sapphire, Lyss, Switzerland) were thoroughly cleaned using Deutracon liquid soap (Decon Laboratories Ltd., East Sussex, UK), Milli-Q distilled water, and acetone. The substrates were dried in the furnace at 300 °C for 15 min to completely eliminate water and acetone. Non-oriented sapphire was used as substrate because it is non-conductive and contributes no additional signal to the transport measurements of the films. The films were deposited on the substrates by a spin coater (Primus STT 15 Northamptonshire, UK) operated at 6000 rpm for 30 s and dried in the furnace at 350 °C for 10 min after a complete coverage.

The optimal conditions to obtain a pure $CaMnO_3$ phase were determined by depositing one coating layer onto the substrate and trying different temperature (700, 800, 900, and 1000 °C) and annealing time (1, 24, and 48 h) combinations. After the definition of standard annealing temperature and time additional layers were applied successively onto the substrate to achieve good coverage. An ideal coverage of the substrate was obtained after four depositions with two different thermal annealing procedures (A and B) described below:

(A) Each layer was applied by spin coating, dried in the furnace at 350 °C for 10 min, and treated at 900 °C for 1 h. This layer deposition sequence was repeated four times. After application of the fourth layer, the sample was annealed at 900 °C for 48 h.

(B) Each layer was applied by spin coating, dried in the furnace at 350 °C for 10 min, and then annealed at 900 °C for 48 h. This procedure was repeated with all four layers.

In both thermal annealing (route A and B) each step was monitored by X-ray diffraction (XRD) in grazing incidence as well as scanning electron microscopy (SEM). With both routes, the best result (pure phase, high crystallinity) was achieved by annealing the samples 48 h at 900 °C.

For the phase identification and the monitoring of the crystallites growth, a PANalytical X'Pert PRO MPD H-2Hx-ray diffractometer (Almelo, Netherlands) was used in grazing angle mode [grazing incidence XRD (GIXRD)] with a PIXCEL detector. One-layer films were measured with a step size of 0.05° and 3 s per step, and the four-layer films with a step size of 0.05° and 130 s per step.

The SEM observation of the microstructure and thickness was done using a FEI NovaNanoSEM 230 (Hillsboro, OR). Scanning transmission electron microscopy in bright and dark field modes (STEM-BF and STEM-HAADF) and transmission electron microscopy (TEM) were performed using a Jeol JEM FS2200 (Tokyo, Japan) with in-column filter. The local composition of the films was checked by electron dispersion x-ray spectroscopy (EDS) and processed by the Jeol JED-2300 software. The cross-sectional area of the film was prepared by a tripod method, and the final electron transparency was achieved by Ar-Ion milling in a Bal-Tec RES 101.

The Seebeck coefficient, electrical resistivity, and power factor (S^2/q) were measured in the range of 300 - 1000 K by a four-point method using a RZ2001i thin film apparatus (Ozawa Science Co., Ltd., Nagoya, Japan) [14,15].

3.2 Synthesis and crystal growth of $CaMn_{0.98}Nb_{0.02}O_{3-\delta}$

Polycrystalline perovskite-type $CaMn_{0.98}Nb_{0.02}O_{3-\delta}$ precursor powders were prepared by a soft-chemistry synthesis method [18]. The resulting powder was densified, packed into latex tubes and hydrostatically pressed at 400 MPa. High-density green body rods with 0.8-1.4 cm in diameter and 10-15 cm in length were obtained and mounted vertically in an aluminum oxide tube. They were heated to 1473 K at a rate of 300 K/h and sintered at this temperature for 15 h for further densification. A density higher than 92% of theoretical density was achieved. Single crystals (approx. 70 mm long and 3 mm diameter) were grown in a four-mirror TSFZ (10000-H, Crystal Systems Corp., Japan) with four 300 W halogen lamps as heating sources. The homogeneity of the molten zone was maintained by clockwise and counterclockwise rotation at 20 rpm of the feed rod and seed rod, respectively. Crystal growth was performed at a pressure of 500 kPa with an Ar and O_2 flow rate of 0.4 L/min and 0.1 L/min, respectively. This high pressure is applied to prevent evaporation [19]. In order to obtain high-quality crystals a slow growth rate of 4 mm/h was used. The growth conditions were adjusted according to previous specifications [20] and the phase diagrams of the Ca-Mn-O [19,21,22] and the $CaMn_{1-x}Mo_xO_3$ [23] system.

The oxygen contents of the sintered rod and the single crystals were analyzed by thermo gravimetric analysis (TGA) using a Netzsch STA 409 CD thermobalance. The sample was heated up to 1373 K at a rate of 10 K/min in a 20% H_2-He atmosphere. Under these conditions, the sample is reduced according to eq. (1) assuming that the final products are in their most stable oxidation states:

$CaMn_{0.98}Nb_{0.02}O_{3-\delta}(s) + (0.97-\delta)\ H_2 \rightarrow CaO(s) + 0.98\ MnO(s) + 0.01\ Nb_2O_5(s) + (0.97-\delta)\ H_2O\ (g)$ **Eq. 1**

Phase purity and crystallinity of the calcined and sintered powders were checked by powder X-ray diffraction (PXRD) using a PANalytical X´Pert PRO θ-2θ scan system. Also, a central piece of the crystal ingot was crushed to powder and subjected to PXRD analysis. The diffraction patterns were collected in the range of 20˚ < 2θ < 100˚ with an angular step interval of 0.0167˚. Lattice parameters, atomic positions and thermal factors as well as bond-length and inter-atomic distance were derived from the XRD patterns by Rietveld refinement using the software *Fullprof* [24]. The Thompson-Cox-Hastings pseudo-Voigt function was chosen to describe the peak shape. The crystallographic orientation of the crystal was determined by the Laue method. For this purpose, the single crystal was cut transversally into pieces of approximately 3 mm diameter and 5 mm long at different positions. The X-ray reflections were recorded by two CCD cameras (Photonic Science Ltd., U.K.). The orientation of the crystal was determined using the simulation program *Orient Express* [25]. Single-crystal diffraction patterns were recorded on a STOE IPDS-2T imaging plate diffractometer operating with Mo-Kα radiation. A total set of 240 frames using two different ϕ angles and $\Delta\omega = 1°$ was recorded. The distance between imaging plate and sample was set to 45 mm resulting in a maximum 2θ of 75°. Peak integration and data processing were carried out with the STOE X-Area program suite (Version 1.54) and structure refinement with the program ShelXL97 [26].

Electron diffraction (ED) and high resolution transmission electron microscopy (HRTEM) were performed using a JEOL-SEM 2200FS with an in-column filter. The local composition was determined by energy dispersive X-ray analysis (EDS). The scanning electron microscope FEI Nova NanoSEM 230 in secondary electron (SE) and backscattered electron (BSE) mode was used together with EDX analysis to distinguish possible phase segregation in the single crystal. The TEM samples of the single crystals were either prepared by a thinning process including mechanical polishing and Ar ion milling to achieve the transparency for TEM analysis, or by suspending fine crushed powder of the crystal in alcohol. For the SEM analysis, a transversal cut of the ingot (3 mm diameter × 4 mm long) was polished to mirror-like quality by mechanical polishing with diamond papers (15, 9, 6, 3 µm).

The Seebeck coefficient of the crystals were measured on bar-shaped specimen (7.5 × 1.6 × 2.82 mm^3) in the temperature range of 0 K < T < 300 K using a *physical property measurement system* (PPMS) from Quantum Design equipped with the thermal transport option (TTO). The measurement was carried out under vacuum (10^{-5} – 10^{-6} mbar).

3.3 Synthesis of polycrystalline $CaMn_{1-x}W_xO_{3-\delta}$ (x = 0.01; 0.03; 0.05)

Polycrystalline perovskite-type phases of $CaMn_{1-x}W_xO_{3-\delta}$ (x = 0.01; 0.03; 0.05) were synthesized by a soft chemistry (SC) method [15]. The SC method provides the reproducible and homogeneous introduction of W into the $CaMnO_3$ lattice. For the preparation of $CaMn_{1-x}W_xO_{3-\delta}$ (x = 0.01; 0.03; 0.05), stoichiometric amounts of $Ca(NO_3)_2{\cdot}4H_2O$ (Fluka, ≥99.0%), $Mn(NO_3)_2{\cdot}4H_2O$ (Merck, 98%), WCl_6 (Aldrich, 99.0%), and citric acid (Alfa Aesar, +98%) were dissolved in 500 ml distilled water to obtain a 0.1 $mol{\cdot}L^{-1}$ solution. The ratio of citric acid to the total concentration of cations (Ca,Mn and W) was 2:1 in order to prevent precipitation. WCl_6 was dissolved in isopropanol prior to addition to the precursor solution to prevent the formation of insoluble WO_3. The solution was polymerized at 353 - 363 K for 4 h under continuous stirring. The polymerized product was transferred to a glass bowl and heated at 353 K overnight. The resulting xerogel precursor was pre-decomposed by heating to 573 K at a rate of 20 K/h. The product was crushed, ground and heated at a rate of 300 K/h to a final temperature of 1373 K where it was calcined for 8 h. The polycrystalline samples were pressed uniaxially using a hydrostatic press before heating them at a rate of 300 K/h to a final temperature of 1473 K where they were sintered for 5 h.

Powder X-ray diffraction (PXRD) patterns were obtained using a PANalytical X´Pert PRO θ-2θ scan system equipped with a Johansson monochromator (Cu-$K\alpha_1$ radiation, 1.5406 Å) and the X'Celerator linear detector. The diffraction patterns were scanned from 20˚ to 100˚

(2θ) with an angular step interval of 0.0167˚. XRD patterns were analyzed by the Rietveld refinement program, *Fullprof* [24], to determine the lattice parameters, atomic positions and thermal factors as well as bond-length and distance between atoms. Thompson-Cox-Hastings pseudo-Voigt functions were chosen as profile function and the instrumental contribution to peak broadening was estimated with the measurement of the standard reference sample CeO_2 (NIST SRM674b).

High resolution transmission electron microscopy (HRTEM) and electron diffraction (ED) studies were carried out using a Jeol JEM FS2200 electron microscope. The morphology of sintered pellets was investigated by scanning electron microscopy (SEM) using a Nova NanoSEM 230 FEI. The oxygen contents were determined by thermogravimetric analysis (TGA) using a Netzsch STA 409 CD [27-29]. ENREF 19 The polycrystalline pellets were heated up to 1373 K at a rate of 20 K/min in reducing atmosphere (20% vol H_2/He) and the weight loss was measured according to:

$$CaMn_{1-x}W_xO_3(s) + H_2 \xrightarrow{1373K} CaO(s) + (1-x)MnO(s) + (x)W(s) + H_2O\ (g) \qquad \textbf{Eq. 2}$$

The Seebeck coefficient and electrical resistivity were measured with a RZ2001i unit from Ozawa Science (Japan) in the temperature range of 300 K < T < 1100 K using rectangular-shaped samples.

The high-temperature thermal conductivity, κ, was determined from measurements of the thermal diffusivity (α), the heat capacity (C_p), and the density (d) using the relationship:

$$\kappa = \alpha * d * C_p \qquad \textbf{Eq. 3}$$

The thermal diffusivities were measured using a Netzsch LFA 457 laser flash apparatus. A Netszch DSC 404 C Pegasus was used to measure the heat capacity (C_p) of the compounds. The compounds were heated up to 1373 K at a heating rate of 20 K/min and a synthetic air flow of 50 mL/min. The C_p was determined by the ratio method from baseline, reference, and sample measurements. The errors shown in Fig. 5, 6, and 7 are based on published data [30].

4. Results and Discussion

4.1. $CaMnO_3$ Thin Films

The conditions for the reproducible synthesis of homogeneous, single phase perovskite-type calcium manganese oxide coatings of the substrates were optimized by systematic parameter variation. Diffraction patterns of one-layer $CaMnO_3$ films obtained at different annealing temperatures and times are shown in Fig. 1 and Fig. 2. From the GIXRD results it can be deduced that $CaMnO_3$ films (ICSD Collection Code: 082211) with the desired quality and no discernible secondary phase were formed after heating at T = 900 °C for 48 h [31, 32]. Other thermal annealing procedures reveal inclusions of Ruddelsden–Popper phases (Ca_2MnO_4) and spinel structures ($CaMn_2O_4$) in the $CaMnO_3$ main phase, as illustrated in the GIXRD pattern of a sample treated at 800 °C for 48 h (Fig. 2).

The GIXRD pattern of the sample annealed at 700 °C in Fig. 1 shows no diffraction peak indicating that the phase was not yet crystallized. Thus, it can be concluded that crystallization of the $CaMnO_3$ layer was not completed at temperatures below 800 °C even after a reaction time of 24 h (Fig. 2).

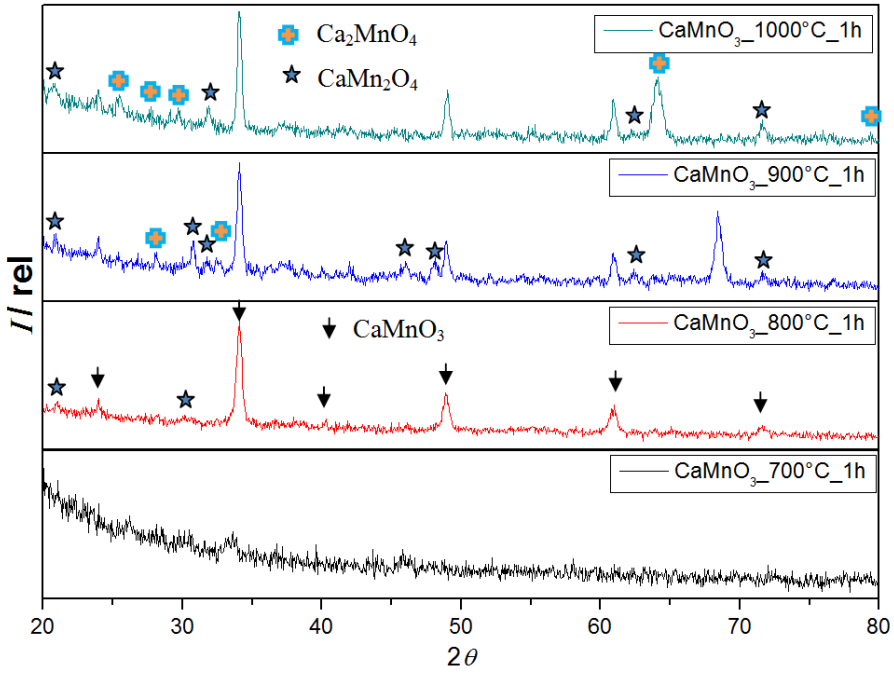

Fig.1. GIXRD patterns of one-layer $CaMnO_3$ films formed at different annealing temperatures.

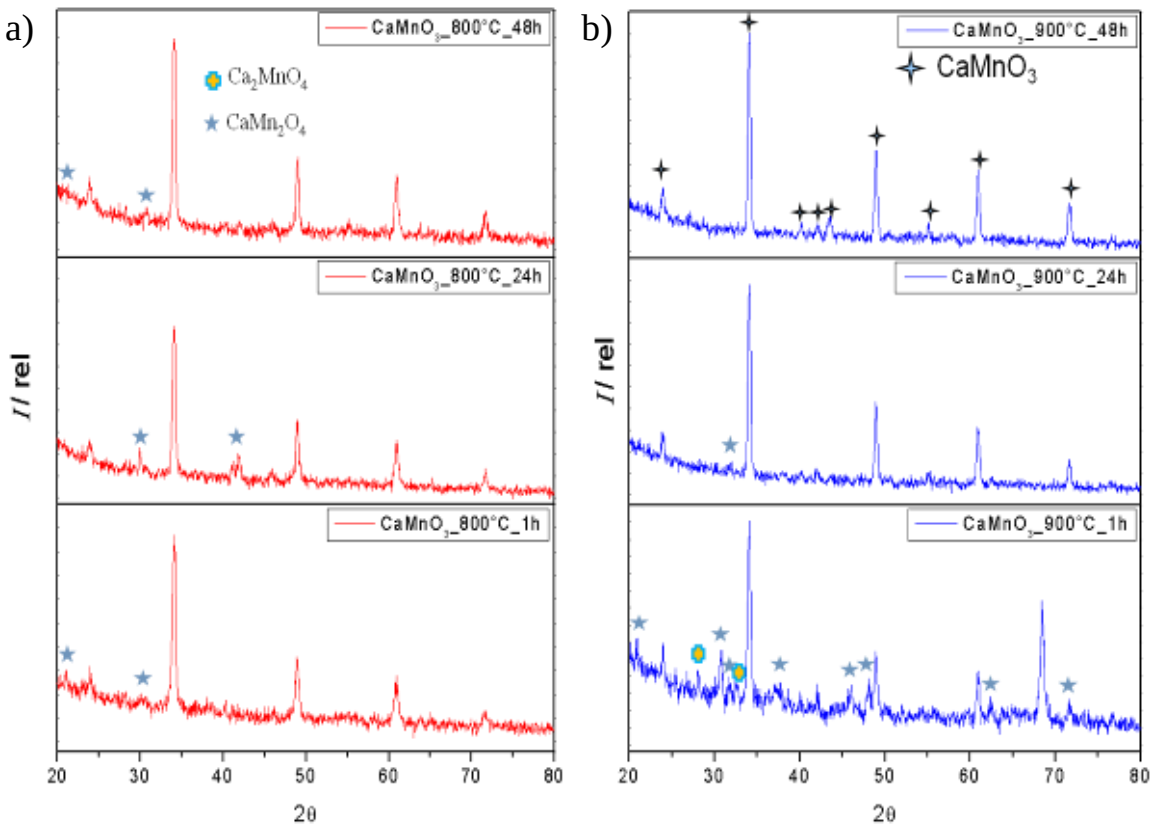

Fig.2. GIXRD pattern of one-layer $CaMnO_3$ films formed at a) 800°C and b) 900°C, respectively, at different annealing times.

The XRD pattern in Fig. 2 reveals the formation of a crystalline perovskite phase already after one hour annealing. At 800 °C, longer treatment leads exclusively to the formation of intermediate secondary phases indicating that the crystallization process is completed after 1 h. At elevated temperatures (T > 900 °C), however, longer thermal annealing (24 h) leads to a considerable reduction of initially formed secondary phases and increases the stability of the film.

GIXRD analysis of the four-layer coatings obtained by route A and B is shown in Fig. 3. Both diffraction patterns exhibit reflections corresponding to $CaMnO_3$ (ICSD Collection Code: 082211) as the main phase. The route B pattern contains impurity reflections in the range of $37° \leq 2\theta \leq 39°$, and in the range of $29° \leq 2\theta \leq 32.5°$ and at 47.5° arising from $CaMnO_{2.75}$ [33] and the spinel $CaMn_2O_4$, respectively (ICSD Collection Code: 062167).

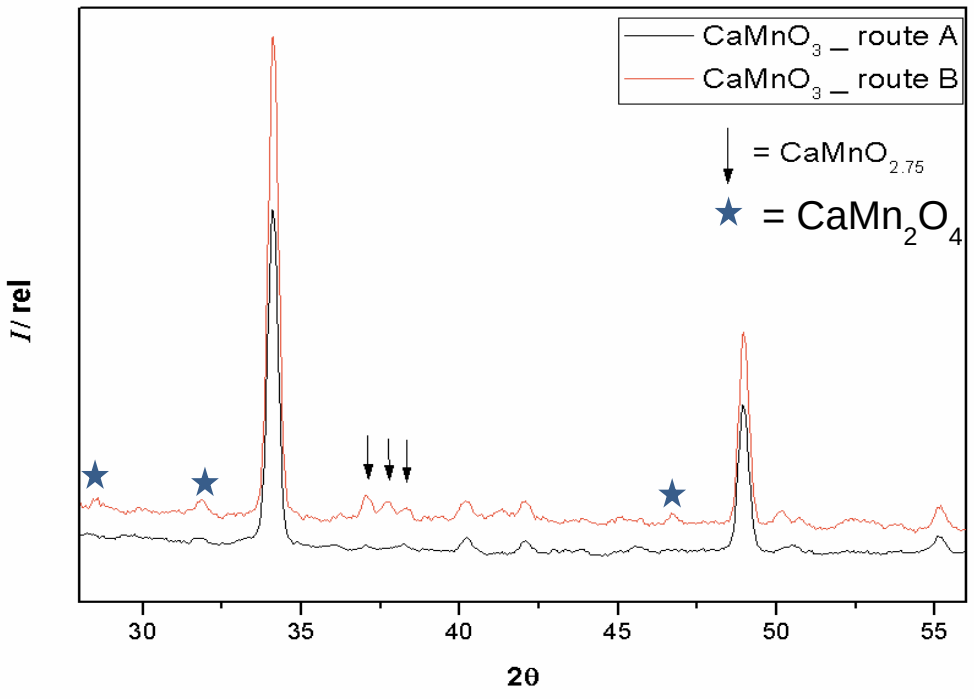

Fig.3. GIXRD patterns of four-layer films obtained by route A and B (in the range of 28° < 2θ < 56° with steps of 0.05° / 130 s).

The surface morphology of the four-layer films obtained by synthesis route A and B can be seen from the SEM images in Fig. 4a and 4b, respectively. Concluding from the XRD and electron diffraction data neither of the films is textured. It is clearly recognizable that synthesis by route A (Fig. 4a) results in a larger grain size than route B (Fig. 4b) which can be explained by different nucleation and growth rates.

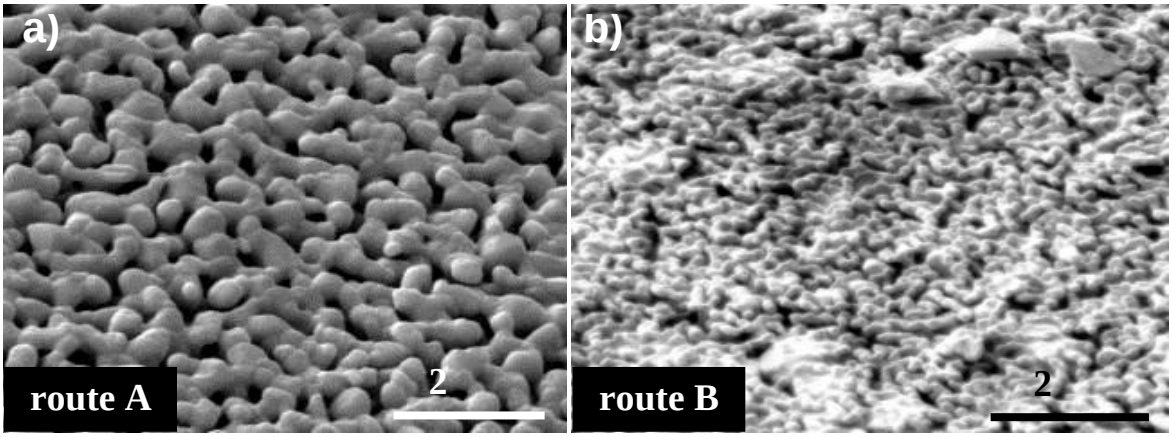

Fig.4. Surface morphology of films obtained by (a) route A and (b) route B.

Fig. 5a shows the TEM bright field (TEM-BF) cross sectional view of a sample obtained by route A. The particle size ranges from 100 to 400 nm, and the total film thickness is 450 to 600 nm. The EDS line scan profile in Fig 5b (taken along the dotted line in Fig.5a) shows that the film homogeneously consists of $CaMnO_3$.. Figure 6a shows a dark field STEM (STEM-DF) cross section image of a four-layer film obtained by route B. The grains are smaller than 200 nm and the thickness ranges from 600 to 700 nm. The EDS cationic composition analysis in Fig. 6b shows a Ca deficiency and slight Mn excess in the midsection of the film

and the difference increases towards the surface [0.62 ≤ (Ca/Mn) ≤ 0.87]. This Mn excess confirms the enrichment of the spinel phase at the grain surface.

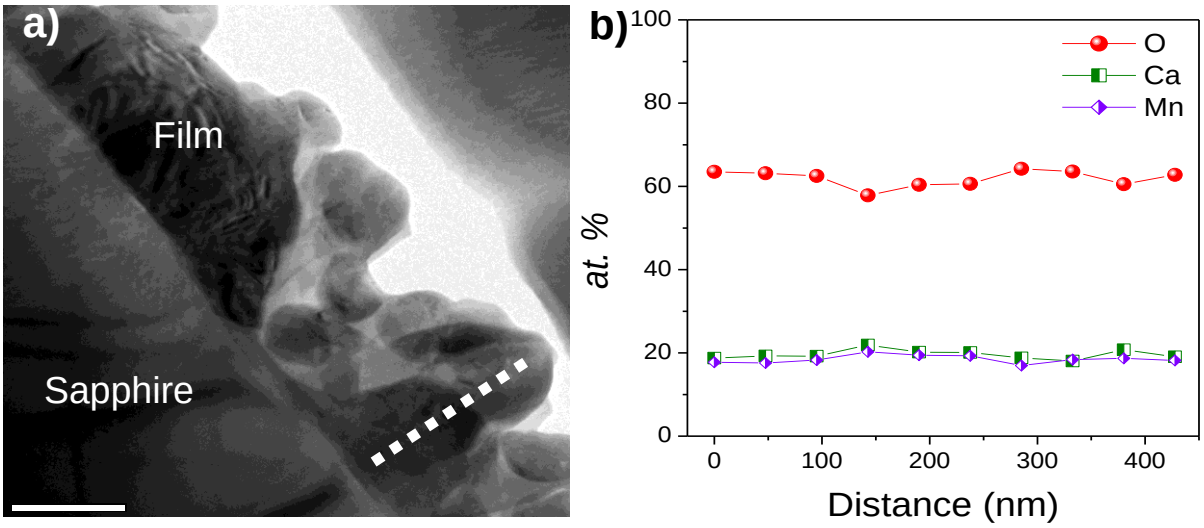

Fig. 5. a) TEM bright field image of the film cross section obtained by synthesis route A with the distinguishable grains; **b)** EDS compositional analysis along the film profile marked in a).

Sintering and complete crystallization of the films requires an annealing temperature of 900 °C (Fig. 1). Therefore, in route A each layer is treated at 900 °C for 1 h initiating the nucleation process, but the short annealing time is insufficient for a complete crystallization of the deposited material. The result is a matrix composed of a few CaMnO3 nucleation sites and not yet crystallized material. Every deposited layer provides more precursor material for the nucleation and the final grain growth is achieved after four deposited layers by a 48-h final thermal annealing. In synthesis route B, each deposited layer is treated 48 h at 900°C. This treatment leads to the formation of many nuclei followed by a grain growth until the available material of the layer is depleted. As a result, the final grain size of route B samples will be smaller than those of route A. In addition, XRD proved that samples synthesized by route B contain some impurities of the spinel phase $CaMn_2O_4$ (Fig. 3). Fig. 6b shows that these impurities are located at the surface of the nanocrystals. Fig. 6c illustrates the difference of the crystallization processes in route A and route B, respectively.

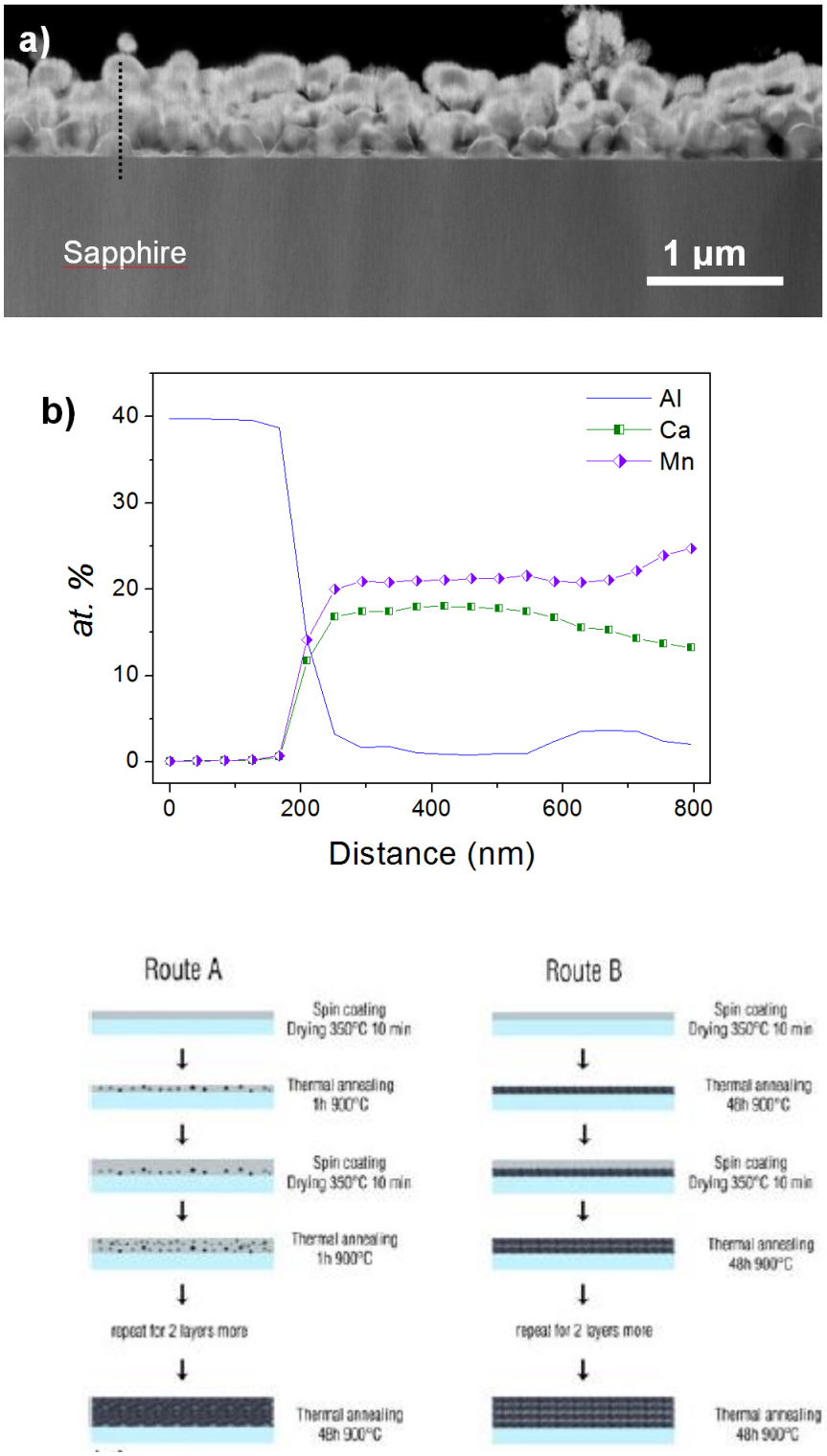

Fig. 6. a) STEM dark field image of the cross section obtained by synthesis route B with distinguishable grains; **b)** EDS compositional analysis along the film profile marked in a); **(c)** Graphical description of the differences between synthesis route A and B.

The thermoelectric properties of four-layer films synthesized by routes A and B are shown in Fig. 7. Films synthesized by both routes A and B have reproducible heating and cooling curves. The Seebeck coefficient (Fig. 7a) is negative in both cases indicating n-type conduction and the values are comparable with bulk samples of the same composition. The electrical resistivity (Fig. 7b) reveals a semiconducting behavior and higher values for

samples prepared by route A. At 1000 K, the electrical resistivities are 0.60 and 0.48 Ωcm for routes A and B samples, respectively. The differences in Seebeck coefficient and resistivity are mainly due to the slight nonstoichiometry of the films prepared by route B. The nonstoichiometry is especially pronounced at the surface of each film layer. The presence of a brownmillerite-type $CaMnO_{2.75}$ phase [33] detected by GIRXD (Fig. 3) could be the origin of the resistivity and Seebeck coefficient reduction. Oxygen deficiency in manganates generates a mixed Mn(IV)/Mn(III) valence responsible for the high electronic conductivity [34] The highest power factor was found at 950 K for films obtained by synthesis route A ($8.5x10^6$ $W/m*K^2$). This value is slightly better than that of bulk $CaMnO_3$ ($6.25 x10^6$ $W/m*K^2$) [35].

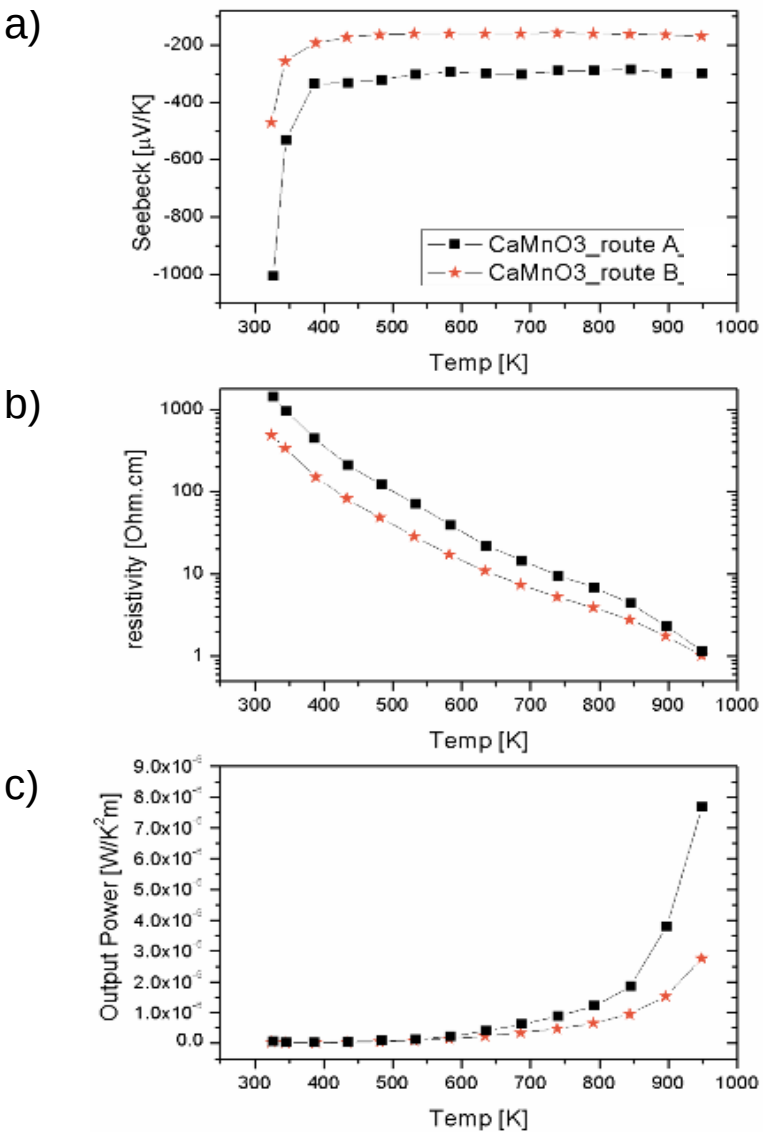

Fig. 7. Temperature dependence of the **a)** Seebeck coefficient; **b)** resistivity and **c)** output power for films prepared by synthesis route A and B, respectively.

4.2. $CaMn_{0.98}Nb_{0.02}O_{3-\delta}$ single crystal

The preparation of high quality rods is a crucial step for successful crystal growth. The precursor powder must be phase-pure and the sintered rods highly compacted. The polycrystalline powder and the sintered $CaMn_{0.98}Nb_{0.02}O_{3-\delta}$ rods were characterized beforehand by PXRD. The measurements confirmed a single phase perovskite structure consistent with previous reports [18, 36]. A high density of the sintered rods prevents suction

from the liquid zone into the feed rod by capillary forces and inhibits gas bubble formations which can lead to zone instability during the crystal growth. After crystal growth, the crystallographic orientation of the ingots was checked by the Laue method. The Laue method revealed single crystals and a [0-10] crystallographic orientation which is confirmed by the HRTEM and ED results. Images of the ingot surfaces (with an approximate diameter of 3 mm) are shown in Fig. 8. SEM-SE images of the central region of the ingot ($0.6 \times 0.3 mm^2$) reveal a homogeneous perovskite-type $CaMn_{0.98}Nb_{0.02}O_{3-\delta}$ single phase (Fig. 8a). The SEM-BSE image in Fig. 8b shows the ingot edge surface with the impurity spinel phase $CaMn_2O_4$ (bright brown part) and $CaMn_{0.98}Nb_{0.02}O_{3-\delta}$ (dark green part) as well as many cracks. The composition was determined by EDX analysis. The BSE mode in SEM allows the determination of compounds according to the atomic number Z. The contrast graduation is caused by the higher relative content of the heavy Mn in $CaMn_2O_4$ than in $CaMn_{0.98}Nb_{0.02}O_{3-\delta}$. EDX studies confirm these compositions in average providing a Nb content of $0.022 \leq x \leq 0.027$ of the perovskite compound. The SEM-BSE image of the same central part of the ingot exhibits the homogeneous perovskite $CaMn_{0.98}Nb_{0.02}O_{3-\delta}$ (8c). The formation of a secondary phase on the ingot edge surface can be explained by the $CaMnO_3$ phase diagram [22]. The liquid crystallizes faster on the edges and surfaces than in the center of the ingot due to the small temperature difference. This faster crystallization on the edges leads to incongruent melting and therefore secondary phases are likely to form [37]. The cracks and striations in the single crystals can also be attributed to this temperature difference mainly due to the phase transition (cubic to orthorhombic at 1000 K) upon solidification during cooling and subsequent strain relaxation [38, 39].

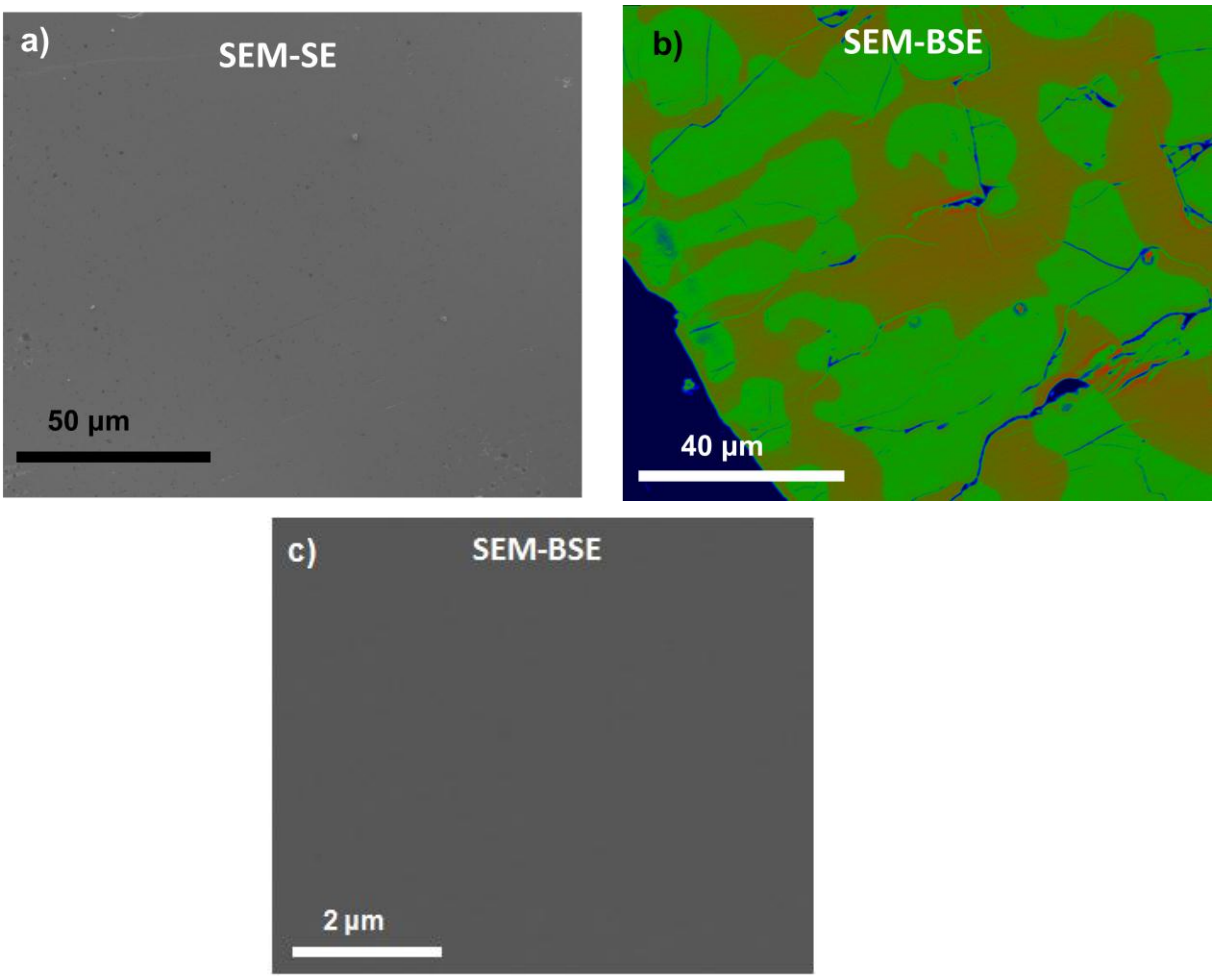

Fig. 8. SEM images of $CaMn_{0.98}Nb_{0.02}O_{3-\delta}$ using **(a)** secondary electron (SE) analysis in the central region of the ingot showing the perovskite single phase; **(b)** backscattering electron (BSE) analysis at the edge of the ingot showing the impurity phase $CaMn_2O_4$ (brighter part) and $CaMn_{0.98}Nb_{0.02}O_{3-\delta}$ (darker part) as well as cracks; **(c)** BSE analysis showing the central part of the ingot free from secondary phases.

The oxygen stoichiometry was calculated using the relative weight loss (r) measured by TGA in reductive atmosphere. The relation between δ and r (Eq. 4) can be established based on the stoichiometry of the decomposition reaction eq. (1):

$$r = \frac{(M_{CaMn_{0.98}Nb_{0.02}O_3} - \delta * M_O) - (M_{CaO} + 0.98 * M_{MnO} + 0.01 * M_{Nb_2O_3})}{(M_{CaMn_{0.98}Nb_{0.02}O_3} - \delta * M_O)} \quad \textbf{Eq. 4}$$

A weight loss *r* of the crystal of 10.56% was determined (Fig. 9). The same result was obtained for the sintered rod material. Using Eq. 4 an oxygen deficiency of $\delta = 0.0235$ is calculated suggesting the chemical composition $CaMn^{III}_{0.04}Mn^{IV}_{0.94}Nb^{V}_{0.02}O_{2.98}$. It is worth to mention that the determined oxygen content is an average value from the central part of the ingot.

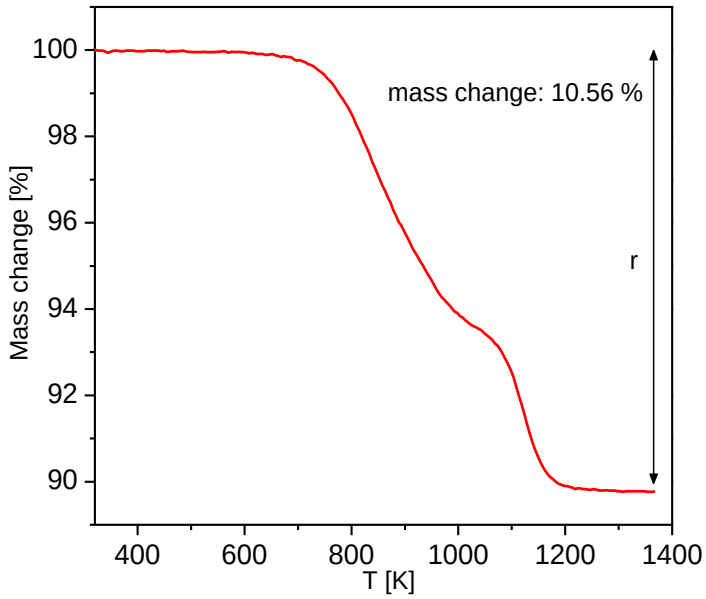

Fig. 9. H_2 reduction TGA curve of the $CaMn_{0.98}Nb_{0.02}O_{3-\delta}$ crystal.

The homogeneous perovskite-type phase of a 0.1 × 0.1 × 0.1 mm^3 piece cut from the central part of the ingot was confirmed by single-crystal X-ray diffraction and SEM. The indexing of the diffraction pattern indicated a primitive cubic cell with a_c = 7.4930(8) Å. The intensity analysis showed that the internal *R* values in both possible cubic Laue classes were unusually high (~ 0.25). Additionally, the suggested space groups $P2_13$ and $P4_232$ are uncommon for perovskite-type oxides. Attempts to find a reference structure in these two space groups were not successful implying a too high symmetry due to twinning. A peak intensity analysis revealed a set of reflections with particularly high intensities. This subset could be indexed using a (pseudo-) tetragonal primitive cell with $\boldsymbol{a} = \boldsymbol{b} = \boldsymbol{a_c}\sqrt{2}$and $\boldsymbol{c} = 2^*\boldsymbol{a_c}$. The observed extinctions suggest a possible orthorhombic space group P*bnm* (non-standard setting of P*nma*) which is in agreement with the Rietveld refinement of the PXRD patterns and widely accepted for calcium manganese oxide (ICSD Collection Code: 082211) [40]. In fact, the structural refinement in this space group immediately led to reasonable results. The inclusion of a second twin domain according to the transformation matrix:

$$\begin{pmatrix} 0 & 1 & 0 \\ 1 & 0 & 0 \\ 0 & 0 & -1 \end{pmatrix} \qquad \textbf{M 1}$$

resulted in already acceptable residual parameters of R_1 = 0.037 and wR_2 = 0.087. On the other hand, the presence of a second set of weaker reflections clearly indicates that a more complex twinning has to be taken into account. This problem has already been discussed for Ca-substituted $LaMnO_3$ by *Van Aken et al.* [41]. The key idea of the twinning model is that the long axis of the orthorhombic-perovskite structure can be oriented along any of the three orthogonal axes, in turn giving rise to the apparent cubic cell symmetry. For any of these three orientations two twin domains exist, which are correlated by an exchange of *a* and *b* and the inversion of *c* according to M 1 (correspondingly, an exchange of *a* and *c* and the inversion of *b* for the P*nma* space group). This results in a six-fold twin, leading to a strong overlap of the signals from the different domains. Since we chose to use the non-standard space group P*bnm*, the resulting transformation matrices for the axes and *hkl*-values differ from those in [16] and are therefore listed below:

$$M1=\begin{pmatrix}-1/2 & 0 & 1/2\\ 1/2 & 0 & 1/2\\ 0 & 1 & 0\end{pmatrix}\quad M2=\begin{pmatrix}1/2 & 0 & 1/2\\ -1/2 & 0 & 1/2\\ 0 & -1 & 0\end{pmatrix}$$

$$M3=\begin{pmatrix}0 & 1/2 & -1/2\\ 0 & 1/2 & 1/2\\ 1 & 0 & 0\end{pmatrix}\quad M4=\begin{pmatrix}0 & 1/2 & 1/2\\ 0 & 1/2 & -1/2\\ -1 & 0 & 0\end{pmatrix}$$

M 2

$$M5=\begin{pmatrix}1/2 & 1/2 & 0\\ -1/2 & 1/2 & 0\\ 0 & 0 & 1\end{pmatrix}\quad M6=\begin{pmatrix}-1/2 & 1/2 & 0\\ 1/2 & 1/2 & 0\\ 0 & 0 & -1\end{pmatrix}$$

A program was written that reads these transformation matrices and generates the corresponding intensity file in the ShelX HKLF 5 format. Data assessments showed that there are sets of signals with the contributions of all six twin domains, while there are other signals with contributions of four or only two domains. This partial merohedral twin structure allows determination of the fractions of the individual twin domains. During refinement it turned out that the two twin domains corresponding to the above-mentioned matrices M5 and M6 contribute only about 1.5% and 2.5%, respectively to the signals. Therefore, these domains were disregarded in the final runs. Since the Nb content in the crystals is very small (0.02 mole ratio) no attempts were made to refine the Mn/Nb site occupation. Instead, all positions were refined using the nominal composition $CaMn_{0.98}Nb_{0.02}O_3$. The obtained R_1 values of 0.039 for reflections with I > 2sigma and 0.054 for all reflections are in the expected range proving the applied structural model correct. The rather large wR_2 values given in Table I are due to a different data handling of files with HKLF 4 and HKLF 5 format in ShelXL. In HKLF 4 files all equivalent reflections are merged, which does not apply for HKLF 5 files. This results in much higher R_1 and wR_2 values as can easily be verified by adding the code MERG 0 in any ShelXL instruction file.

The results of the structure refinement are listed in Tables I-III. Selected bond lengths and angles are specified in Table IV. Fig. 10 shows a representation of the crystal structure viewed along the ***c*** axis (in P*bnm* settings). Anisotropic displacement parameters are depicted with a 90% probability. Analysis of the Mn/Nb–O bond lengths reveals a nearly tetragonal site symmetry with two bonds being significantly longer (≈ 0.008 Å) than the other four which is expected for the Jahn-Teller active Mn^{3+} ion. However, the Jahn-Teller elongation is not very pronounced since the Nb^{5+} content and therefore also the Mn^{3+} content is small (based on the oxygen content determined by TGA).

It should be noted that almost identical results for atomic positions, displacement parameters and in turn bond lengths and angles were obtained from the refinement of the reduced dataset described above. This proves the approach of six twin domains correct. The crystal was re-measured at 160 K to check for possible phase transitions. It was found that the crystal structure remains basically unchanged, the apparent cubic cell parameter being slightly shorter ($\boldsymbol{a}_c \approx \boldsymbol{c}$ = 7.4852(6)). Especially, no splitting of the diffraction peaks was observed, i.e. the relation $\boldsymbol{a} \approx \boldsymbol{b} \approx \boldsymbol{c}/\sqrt{2}$ is preserved at low temperatures. The Mn/Nb–O bond lengths (Mn/Nb–O1: 1.9053 (3) Å, Mn/Nb–O2: 1.9054(7) Å, Mn/Nb–O2: 1.9142(7) Å) and angles (Mn/Nb–O1–Mn/Nb: 158.33(7)°, Mn/Nb–O2–Mn/Nb: 156.96(5)°) are only slightly modified. Since no prominent changes in the structural parameters were observed, details of the low temperature results are not listed here.

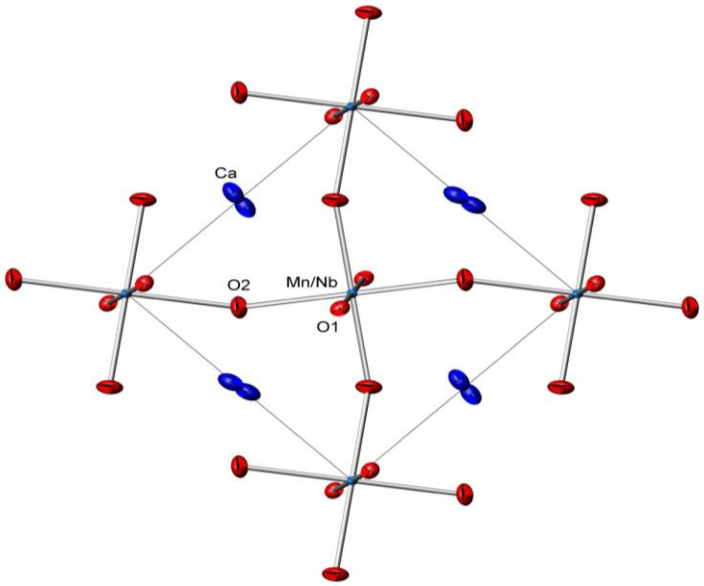

Fig. 10. Crystal structure of $CaMn_{0.98}Nb_{0.02}O_{3-\delta}$ viewed along c based on the crystal refinement parameters. Anisotropic displacement parameters are shown with 90% probability.

The Rietveld refinement results of the powdered center of the ingot (homogeneous part) confirm that $CaMn_{0.98}Nb_{0.02}O_{2.98}$ has an orthorhombic crystal structure with the space group *Pbnm* and the refined crystal structural parameters are shown in Table V. Although $Ca_2Mn_2O_5$ was not detectable by SEM-BSE as a secondary phase, it was detected by PXRD. Quantitative phase analysis (QPA) performed during Rietveld refinement revealed that 8.37% of the $Ca_2Mn_2O_5$ is located in the outer part of the powdered crystal.

Table I. Crystal data and structure refinement of the $CaMn_{0.98}Nb_{0.02}O_{3-\delta}$ crystal.

Diffractometer	STOE IPDS-2T
Temperature	293 K
Wavelength	0.71073 Å
Crystal system, space group	Orthorhombic, Pbnm (#62)
Unit cell dimensions	a = 5.2984(6) Å
	b = 5.2984(6) Å
	c = 7.4930(8) Å)
Volume	210.35(4) $Å^3$
Z, Calculated density	4, 4.540 $g \cdot cm^{-3}$
Absorption coefficient	8.4 mm^{-1}
F(000)	278
Crystal size	0.1*0.1*0.1 mm^3
Theta range for data collection	3.9-37°
Index ranges	$-12 \leq h \leq 12$
	$-12 \leq k \leq 12$
	$-12 \leq l \leq 12$
Reflections collected / unique	2962 / 533
Refinement method	Full-matrix least-squares on F^2
Absorption correction	numerical (6 faces)
Data / restraints / parameters	2792 / 0 / 34
Goodness-of-fit on F^2	0.957
Final R indices [I>2sigma(I)]	$R_1 = 0.0392$, $wR_2 = 0.1284$[a)]
R indices (all data)	$R_1 = 0.0543$, $wR_2 = 0.1334$[a)]
Extinction coefficient	0.041(5)
Largest diff. peak and hole	1.41 and -0.96 $e \cdot A^{-3}$

[a)] $w = 1/[\sigma^2(F_o^2)+(0.0923 *P)^2]$ where $P = (F_o^2+2F_c^2)/3$

Table II. Atomic coordinates and equivalent isotropic displacement parameters of $CaMn_{0.98}Nb_{0.02}O_{3-\delta}$. U_{eq} is defined as one third of the trace of the orthogonalized U_{ij} tensor.

Atom	x	y	Z	SOF	$U_{eq}[Å^2]$
Ca	-0.00572(8)	0.53197(11)	0.75	0.5	0.0070(1)
Mn/Nb	0.	0.	0.5	0.49/0.01	0.0021(1)
O1	0.06660(33)	-0.01370(25)	0.75	0.5	0.0044(3)
O2	-0.28763(21)	-0.21353(22)	0.53342(17)	1.0	0.0074(2)

Table III. Anisotropic displacement parameters ($Å^2$) of $CaMn_{0.98}Nb_{0.02}O_{3-\delta}$.

Atom	U_{11}	U_{22}	U_{33}	U_{23}	U_{13}	U_{12}
Ca	0.0044(2)	0.0088(2)	0.0077(2)	0.	0.	-0.0011(1)
Mn/Nb	0.0020(2)	0.0016(2)	0.0025(2)	0.0005(5)	0.0001(1)	-0.0001(1)
O1	0.0055(7)	0.0041(6)	0.0037(6)	0.	0.	0.0003(4)
O2	0.0055(4)	0.0066(4)	0.0101(4)	0.0001(4)	0.0016(4)	-0.0026(3)

Table IV. Selected inter-atomic distances (Å) and bond angles (°) in $CaMn_{0.98}Nb_{0.02}O_{3-\delta}$.

Name		$CaMn_{0.98}Nb_{0.02}O_{3-\delta}$
Distance		
Mn/Nb-O1	x2	1.9059(11)
Mn/Nb -O2	x2	1.9076(4)
Mn/Nb -O3	x2	1.9145(11)
Ca-O1		2.3392(18)
Ca-O1		2.4376(15)
Ca-O1		2.9164(15)
Ca-O1		2.9815(18)
Ca-O2	x2	2.3504(13)
Ca-O2	x2	2.5851(13)
Ca-O2	x2	2.6021(13)
Angle		
Mn/Nb-O1-Mn/Nb		158.23(10)
Mn/Nb-O2-Mn/Nb		157.43(7)

Table V. Refined structural parameters of the powdered $CaMn_{0.98}Nb_{0.02}O_{3-\delta}$ crystal.

Name		$CaMn_{0.98}Nb_{0.02}O_{3-\delta}$
Diffractometer		PANalytical X´Pert PRO
Radiation source		Lab X-ray $CuK_{\alpha 1}$
Wavelength (Å)		1.5406
Temperature (K)		298
2θ range (^{o})		20 - 100
Space Group		*Pbnm*
a (Å)		5.2744 (1)
b (Å)		5.2924 (1)
c (Å)		7.4692 (1)
V (Å^3)		208.4998
Ca	x	0.9840 (10)
	y	0.0307 (6)
	z	0.25
	B_{iso} (Å^2)	1.05 (6)
	site	4c
	occ.	0.5
Mn/W	x	0.5
	y	0
	z	0
	B_{iso} (Å^2)	0.21 (4)
	site	4b
	occ.	0.49/0.01
O1	x	0.0559 (16)
	y	0.4832 (18)
	z	0.25
	B_{iso} (Å^2)	1.35 (10)
	site	4c
	occ.	0.5
O2	x	0.7048 (13)

	y	0.2802 (16)
	z	0.0325 (11)
	B_{iso} (Å^2)	1.35 (10)
	site	8d
	occ.	1.0
R_p	2.15	
R_{wp}	2.85	
χ^2	2.54	

Fig. 11 shows examples of single-domain perovskite with zone axis: a) [001], b) [100], and c) [110] in *Pbnm* setting ($a \approx b \approx \boldsymbol{a}_p\sqrt{2}$, $c \approx 2\boldsymbol{a}_p$). The presence of twin domains detected by single-crystal X-ray diffraction and the existence of $Ca_2Mn_2O_5$ detected by PXRD was confirmed by HRTEM and ED. Fig. 12 shows the twin domains. In part A, the ***ĉ*** axis of both twin domains, (1) [-110] and (2) [110], are plane perpendicular, while in part B, the ***ĉ*** axis of (2) [110] is in plane and that of (3) [001] out of plane, and both perpendicular to each other. These combinations of twin domains results in a permutation of the ***ĉ*** axis in two (1+2 = A, 2+3 = B) or three directions (A + B = C) in 3D-space as described by single-crystal diffraction analysis with the matrices M1-M6 (Fig. 11 - lower part). Another frequent combination of twin domains is [100] and [010], not shown here.

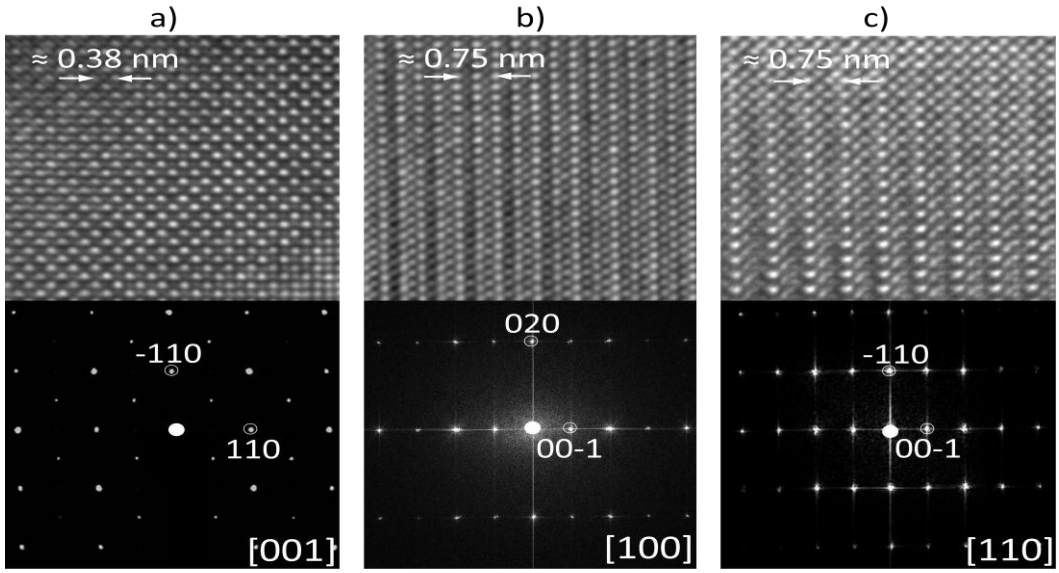

Fig. 11. HRTEM image and ED of single-domain perovskite with zone axis: a) [001], b) [100], and c) [110] in Pbnm setting ($a \approx b \approx a_p\sqrt{2}$, $c \approx 2a_p$).

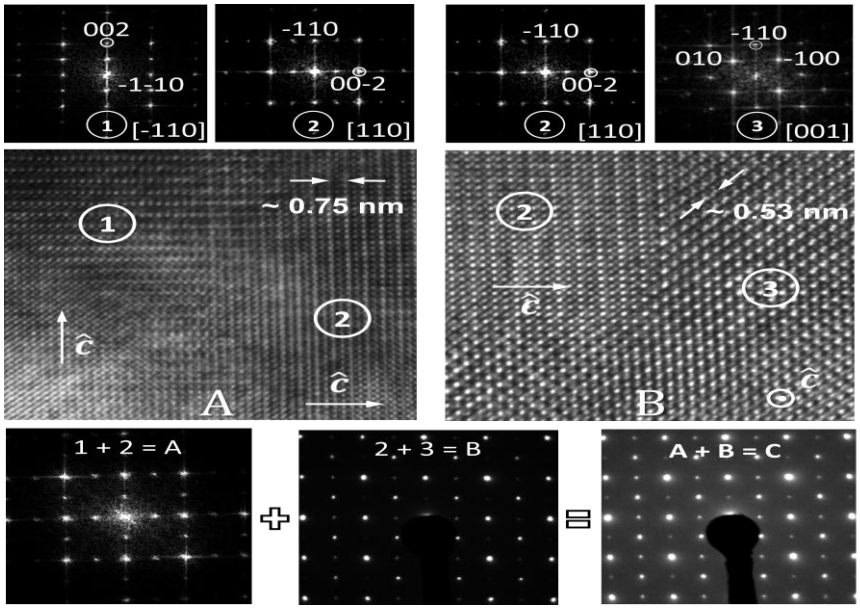

Fig. 12. ED and HRTEM images of twin domains. Image A shows a combination of (1) [-110] and (2) [110] and image B of (2) [110] and (3) [001] twin domains. The combinations of three twin domains gives rise to a permutation of the ***ĉ*** in the three directions of space (A+B=C).

$CaMnO_{2.5}$ was also detected by HRTEM as minor phase in several particles, in diverse orientations and inter-grown with the main component $CaMn_{0.98}Nb_{0.02}O_{3-\delta}$. Fig. 13 shows the [101] zone axis HRTEM image of $CaMn_{0.98}Nb_{0.02}O_{3-\delta}$, where the direction <010> presents an intergrowth superstructure diffraction corresponding to ($\sqrt{2}$ x 4$\sqrt{2}$) $\boldsymbol{a}_p$ R45º oxygen vacancy order. This vacancy order creates a superstructure with extra diffraction spots in (1/4, k, l) which is described in detail in [42]. It is assumed that the superstructure of the brownmillerite-like $AMO_{2.5}$ consist of n-1 perovskite-like layers of MO_6 octahedra (with n = 4) separated by single layers of MO_4 tetrahedra.

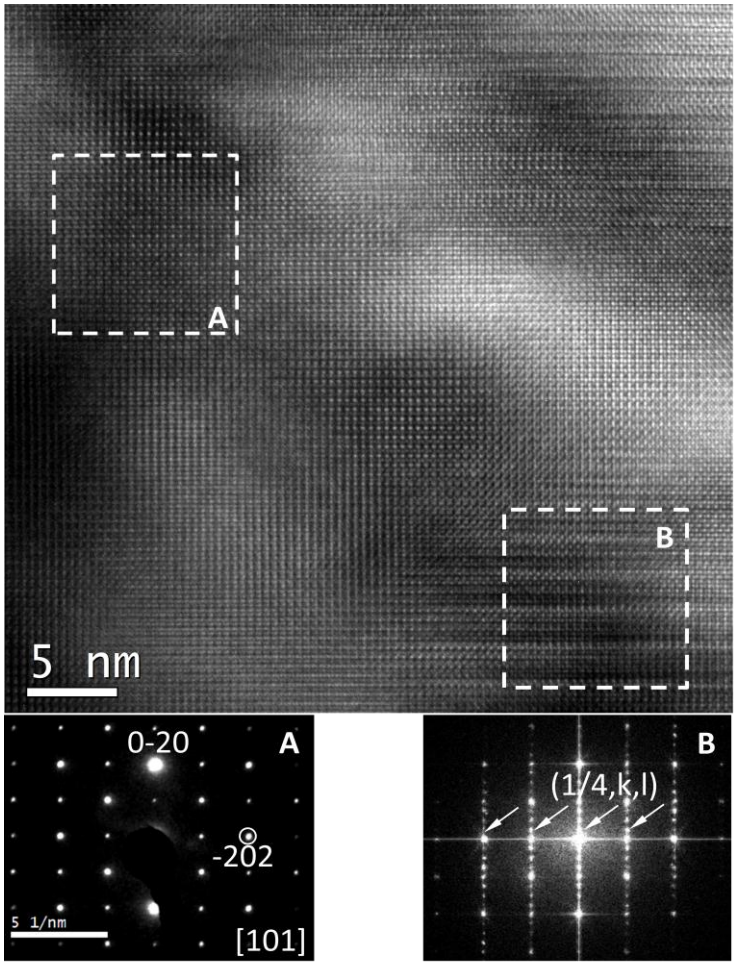

Fig. 13. HRTEM image of $CaMn_{0.98}Nb_{0.02}O_{3-\delta}$ along the [101] zone axis intergrown with $Ca(Mn,Nb)O_{2.5}$ with oxygen vacancy order giving rise to a superstructure ($\sqrt{2}$ x $4\sqrt{2}$) a_p R45º.

Fig. 14 shows the temperature dependence of a) the Seebeck coefficient, and b) the thermal conductivity of both single-crystalline and polycrystalline $CaMn_{0.98}Nb_{0.02}O_{3-\delta}$ in the temperature range of 0 K < T < 300 K. The Seebeck coefficient (Fig. 7a) is negative with a high absolute value of $|S| \geq 100$ µV/K in the whole range indicating that both samples are n-type semiconductors. The maximum at 125 K indicates a transition to antiferromagnetic ordering [43]. This transition also influences the Seebeck coefficient. Around this temperature, the samples display colossal magnetoresistance (CMR) when exposed to a magnetic field which is common for calcium manganese oxides [44]. The Seebeck curve of the polycrystalline compound [36, 45] shows a similar slope as that of the crystal. However, the crystal exhibits slightly lower absolute values than the polycrystalline sample at 300 K ($S_{\text{single crystal}}$ = -145 µV/K and $S_{\text{polycrystalline}}$ = -181 µV/K, respectively). Ideally, the Seebeck coefficient of single crystals and polycrystalline samples should follow Heikes formula ($S_H = -k_b/e \ln[(1 - x)/x]$), where S_H is Heikes' Seebeck coefficient, k_b is the Boltzmann constant, e is the elementary charge, and x the charge carrier concentration [46-48]. However, the measured values are higher than the calculated Heikes' coefficient S_H (-123.376 µV/K). Thus the Heikes formula is not valid for these samples. The deviation could originate from the different Mn contents of single crystals and polycrystalline samples. During crystal growth, some of the Mn evaporates from the melted rods. This is a common process and was previously reported for $La_{1-x}Sr_xMnO_3$ [49], and $CaMn_{1-x}Mo_xO_{3-\delta}$ [23]. Thus, the single crystal has a lower Mn content than the polycrystalline sample leading to a higher conductivity due to charge imbalance in the compound and thereby to a lower Seebeck coefficient.

The thermal conductivity of the single crystal (Fig. 7b) is higher than that of the polycrystalline sample at 300 K ($K_{\text{single crystal}}$ = 5 W/mK and $K_{\text{polycrystalline}}$ = 3.5 W/mK) due to the

elimination of grain boundaries. This means that phonons can travel faster in the single crystals than in polycrystalline samples. However, the values are lower compared to the reported thermal conductivity of un-substituted $CaMnO_3$ single crystals at 300 K (K_{CaMnO3} = 6 W/mK) [50, 51]. Phonon scattering increases in the Nb substituted $CaMnO_3$ single crystals due to increased local lattice distortions caused by the presence of Nb atoms in $CaMnO_3$ matrix, as previously reported [5, 52].

The cracks inside the sample made it impossible to measure the electrical resistivity. Millimeter-thin cracks and striations appear randomly in the single crystal. In contrast to the sintered rods, several attempts to measure the electrical resistivity of the single crystal produced inconsistent results. Efforts to eliminate the cracks (i.e. slower growing rates (0.3-2.9 mm/h), re-calcination at high pressure (1100 K at 500 kPa), slow cooling after crystal growth (cooling rate 0.5-2 K/h) were without success. Though the number of cracks could be reduced, they were not completely eliminated which is in agreement with previous reports [23]. The existing cracks, however, do not influence the Seebeck coefficient and thermal conductivity.

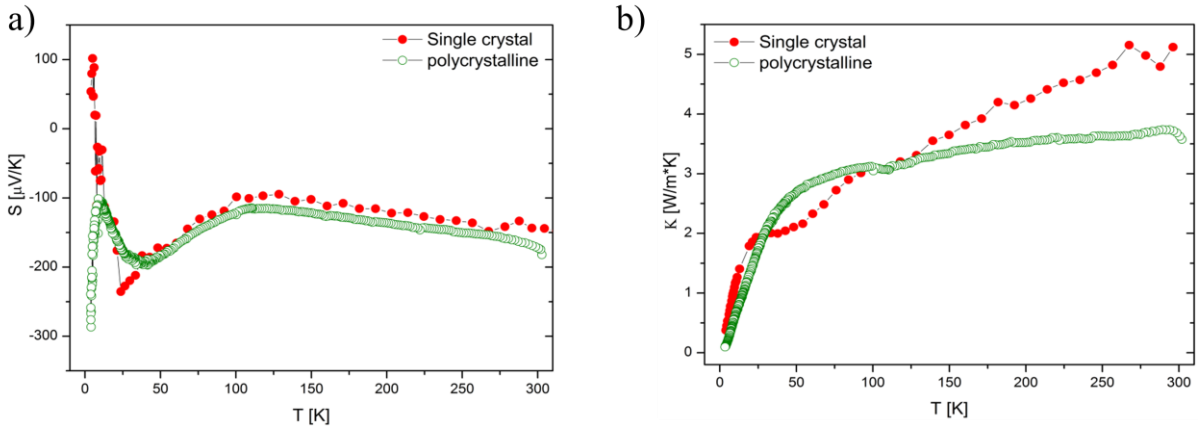

Fig. 14. Temperature dependence of a) Seebeck coefficient, b) thermal conductivity of the single crystal and the polycrystalline material.

4.3 Polycrystalline CaMn1-xWxO3-δ (x = 0.01; 0.03; 0.05)

The XRD pattern of $CaMn_{0.99}W_{0.01}O_{3-\delta}$ and the Rietveld refinement shown in Fig. 15 affirm a single- phase perovskite structure. A graphic representation of the crystal structure is shown in the inset. It reveals a slight distortion of the orthorhombic lattice due to increased unit cell volumes, bond lengths, and bond angles as a consequence of the substitution of W for Mn. The diffractions can be indexed as orthorhombic with *Pnma* space group and the refined structural parameters of all compounds are summarized in Table VI.

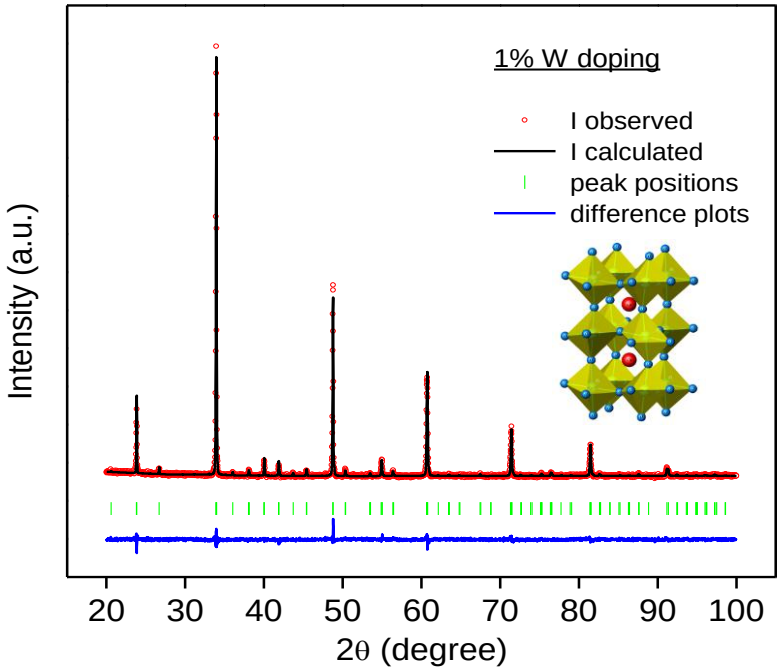

Fig.15. Rietveld refinement of $CaMn_{1-x}W_xO_{3-\delta}$ (x = 0.01) **Inset:** Crystal structure of $CaMn_{0.97}W_{0.03}O_{3-\delta}$.

Table VI. Refined crystal structural parameters for $CaMn_{1-x}W_xO_{3-\delta}$ (x = 0.01; 0.03; 0.05).

Name		$CaMn_{0.99}W_{0.01}O_{3-\delta}$	$CaMn_{0.97}W_{0.03}O_{3-\delta}$	$CaMn_{0.95}W_{0.05}O_{3-\delta}$
Radiation source		$CuK_{\alpha 1}$	$CuK_{\alpha 1}$	$CuK_{\alpha 1}$
Wavelength (Å)		1.5406	1.5406	1.5406
Temperature (K)		298	298	298
2θ range (^{o})		20 - 100	20 - 100	20 - 100
Space Group		*Pnma*	*Pnma*	*Pnma*
a (Å)		5.2868(1)	5.2997(1)	5.3101(1)
b (Å)		7.4645(1)	7.4771(1)	7.4874(2)
c (Å)		5.2749(1)	5.2830(1)	5.2937(1)
V (Å^3)		208.167(7)	209.343(7)	210.470(8)
Ca	*x*	0.02804(5)	0.0316(5)	0.0308(4)
	y	1/4	1/4	1/4
	z	0.0053(19)	0.0062(15)	0.0057(14)
	B_{iso} (Å^2)	0.61(6)	0.71(5)	1.13(4)
	Site	4c	4c	4c
	g	0.5	0.5	0.5
Mn/W	*x*	1/2	1/2	1/2
	y	0	0	0
	z	0	0	0
	B_{iso} (Å^2)	0.66(0)	0.66(0)	0.66(0)
	Site	4b	4b	4b
	g	0.495/0.005	0.485/0.015	0.475/0.025
O1	*x*	0.4888(17)	0.4884(16)	0.4888(12)
	y	1/4	1/4	1/4
	z	-0.0685(35)	-0.0681(22)	-0.0669(23)
	B_{iso} (Å^2)	1.76(9)	1.08(8)	1.82(7)
	Site	4c	4c	4c

	g	0.5	0.5	0.5
O2	*x*	0.2908(14)	0.2843(14)	0.2824(12)
	y	0.0298(16)	0.0314(12)	0.0331(12)
	z	0.2890(19)	0.2912(13)	0.2895(12)
	B_{iso} (Å^2)	1.76(9)	1.08(8)	1.82(7)
	site	8d	8d	8d
	g	1.0	1.0	1.0
R_p		2.48	2.46	5.25
R_{wp}		3.22	3.19	6.75
R_{exp}		2.37	2.40	4.92
χ^2		1.85	1.76	1.88

Numbers in parentheses are standard deviations

g: occupation factor

R_p, R_{wp}, R_{exp}, and χ^2 are the reliability factors and goodness-of-fit, respectively

The substitution of W for Mn produces distortions recognized by an increase of the unit cell volume (Fig. 16) which is in agreement with previous reports [53]. The distortion arises from the larger ionic radii of W^{6+} and Mn^{3+} generated in the Mn^{4+} site (ionic radii of W^{6+}, Mn^{3+}, Mn^{4+} are 0.74, 0.645, and 0.53 Å, respectively) [54]. Thus, the average Mn-O bond length and the unit cell volume of the crystal increase with increasing W content (Fig. 16a and 16c, respectively). In addition, the average <Mn-O-Mn> bond angle increases (Fig. 16b) enhancing the octahedral distortion from the cubic aristotype perovskite.

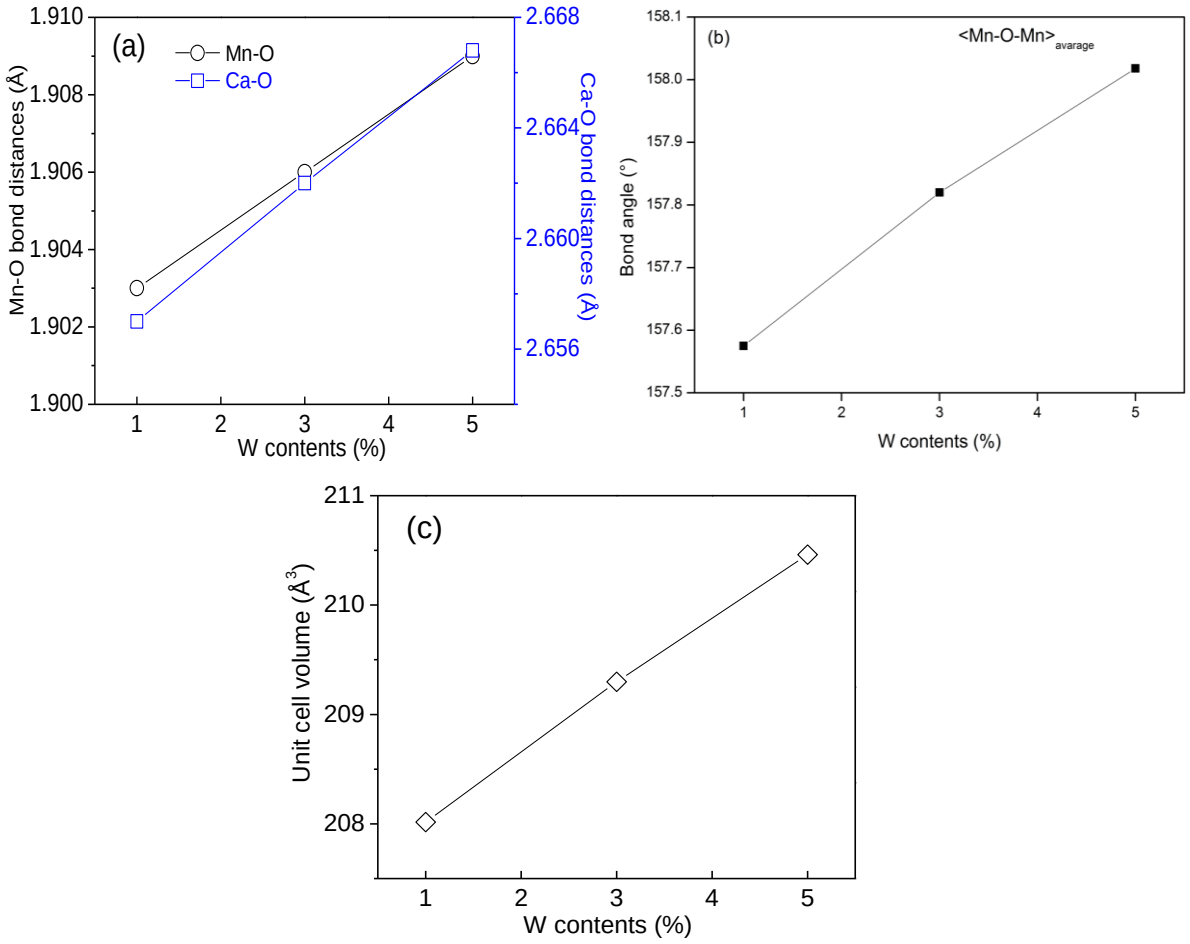

Fig. 16. Plots of **(a)** average bond lengths, **(b)** average bond angles, and **(c)** average unit cell volumes as a function of the W content.

The typical morphology of sintered samples synthesized by a SC method is shown in Fig. 17. They have relative densities of 79% to 84% and grain sizes of 400 to 800 nm. The grains are well interconnected and form porous platelet layers. Sintering resulted in high relative densities which is important for the improvement of the thermoelectric and mechanical properties of the material.

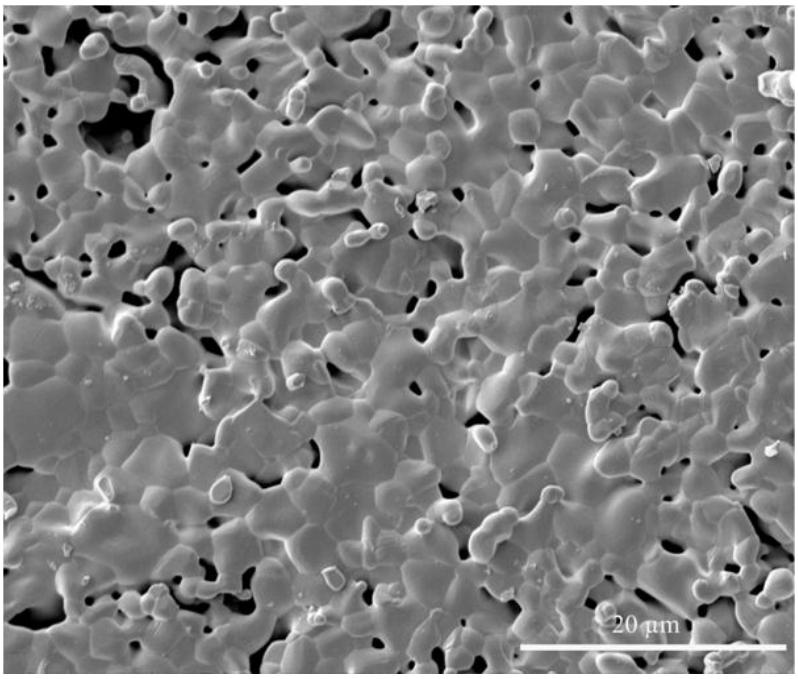

Fig. 17. SEM image of $CaMn_{0.97}W_{0.03}O_{3-\delta}$ with a density of 84%.

A typical HRTEM image of twinned domains is shown in Fig. 18 as previously reported [55, 56]. The superposition of two zone-axis, $[10\text{-}1]_o$ and $[101]_o$, corresponding to the orthorhombic structure were identified by Fast Fourier Transform of different regions using Digital Micrograph 3.8.2 (Gatan). The usual domain size is in the range of 30-50 nm. Twinning occurs during cooling because $CaMnO_3$ undergoes a transition from the higher symmetrical cubic structure at high temperatures (≥1000 K) to the lower symmetrical orthorhombic structure at low temperatures. The orthorhombic unit cell of $Ca(Mn/W)O_3$ is characterized by the lattice parameters $a \approx \sqrt{2}a_p$, $b \approx 2a_p$, and $c \approx \sqrt{2}a_p$, where a_p is the parameter of the cubic perovskite. Therefore, areas with different orientations of the unit cell but related to a_p can grow together resulting in a coherent unit and the phenomenon of twinned domains [56, 57]. Twin domains play a role in reducing the thermal conductivity by increasing phonon scattering [58].

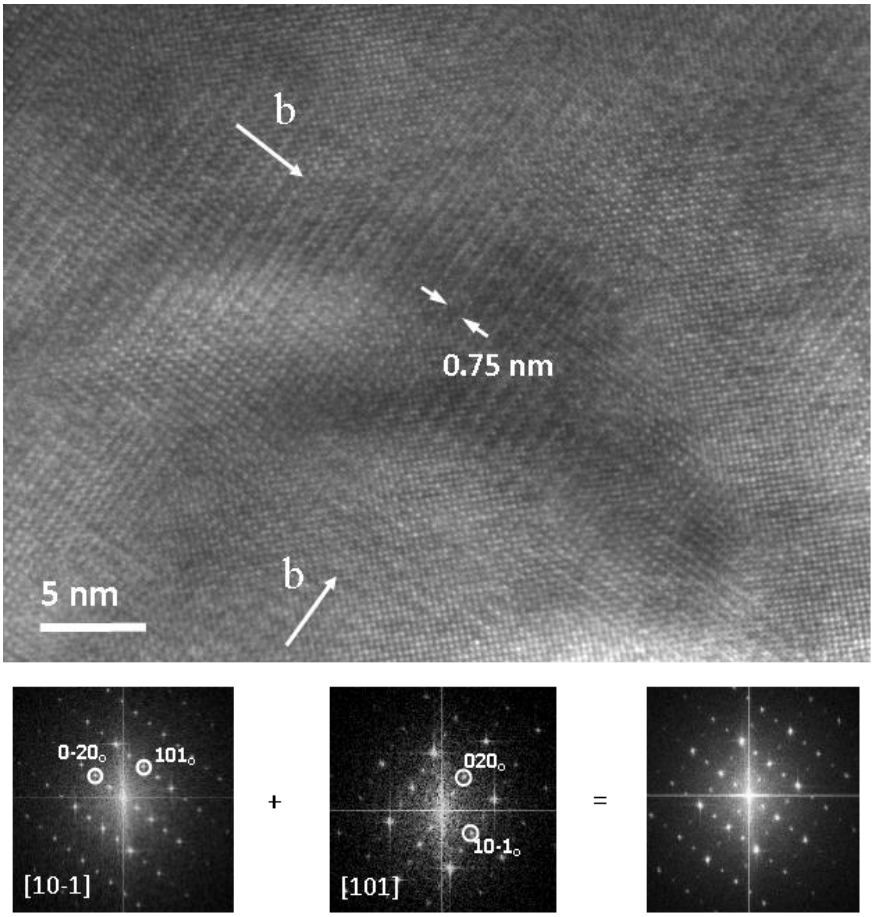

Fig. 18. HRTEM image of $CaMn_{1-x}W_xO_3$ showing the twin domain structure ([10-1] and [101] zone axis) typical for distorted perovskite compounds. FFT was used to determine the different orientations of the unit cells in the twin domains and to resolve overlapping reflections.

TGA reveals oxygen deficiencies for all $CaMn_{1-x}W_xO_{3-\delta}$ samples as shown in Table VII. In defect-free $CaMnO_3$ the Mn^{4+} cation is surrounded by six oxygen anions in octahedral coordination. However, in oxygen-deficient structures two neighboring Mn^{4+} ions are reduced to Mn^{3+} to maintain the charge balance. At δ = 0.5 all Mn^{4+} ions are reduced to Mn^{3+} and surrounded by oxygen in square pyramidal coordination [59]. The creation of Mn^{3+} cations increases the electrical conductivity of the samples [43, 60].

Table. VII. B-site cationic compositions, oxygen content, and relative densities of $CaMn_{1-x}W_xO_{3-\delta}$ (x = 0.01; 0.03; 0.05).

Tungsten / Niobium substitution	Cationic composition	Oxygen content	Relative densities
0.01	$CaMn^{III}_{0.098}Mn^{IV}_{0.892}W^{VI}_{0.01}O_{3-\delta}$	2.961	~ 81 %
0.03	$CaMn^{III}_{0.284}Mn^{IV}_{0.686}W^{VI}_{0.03}O_{3-\delta}$	2.888	~ 84 %
0.05	$CaMn^{III}_{0.458}Mn^{IV}_{0.492}W^{VI}_{0.03}O_{3-\delta}$	2.821	~ 79 %

Fig. 19a shows the electrical resistivity of $CaMn_{1-x}W_xO_{3-\delta}$ (x=0.01; 0.03; 0.05) in the temperature range of 300 K < T < 1000 K. The electrical resistivity of all compounds increases with increasing temperature, thus showing a metallic behavior. It can also be seen that the electrical resistivity of the compounds decreases with increasing W substitution. For instance, at 1000 K $CaMn_{0.95}W_{0.05}O_{3-\delta}$ has the lowest electrical resistivity of all compounds

with $\rho_{5\%W}$ = 7.5 mΩ cm. The replacement of Mn(IV) with W(VI) cations introduces more charge carriers and generates a Mn^{4+}/Mn^{3+} network in which electrons can hop from Mn^{3+} to Mn^{4+} sites mediated by the oxygen 2p electrons [61]. This phenomenon is commonly known as double exchange (DE) mechanism [44, 53, 62].

A correlation of Seebeck coefficient and W substitution in $CaMn_{1-x}W_xO_{3-\delta}$ (x = 0.01; 0.03; 0.05) is evident from Fig 19b. All compounds exhibit large negative Seebeck coefficients indicating that electrons are the predominant charge carriers in the temperature range of 300 K < T < 1000 K. At 1000 K, $CaMn_{0.99}W_{0.01}O_{3-\delta}$ has the highest absolute value of all W substituted samples (S = -270 µV/K). The Seebeck coefficient of the $CaMn_{1-x}W_xO_{3-\delta}$ compounds decreases with increasing W substitution due to increasing charge carrier concentration, as previously reported [16, 44, 63].

Since the Seebeck (S) coefficient is an intrinsic material property that can be influenced by the degree of substitution, thus depending on the composition of the sample, it should follow Heikes formula ($S_H = -k_b/e \ln[(1 - x)/ x]$) at high temperatures (where S_H is Heikes Seebeck coefficient, k_b is the Boltzmann constant, e is the elementary charge, and x is the charge carrier concentration) [47, 64, 65]. However, for small W substitutions levels, the absolute values of the calculated coefficients S_H are higher than the measured values (e.g. for 1% W substitution, S_H = -374 µV/K while S_{exp} = -270 µV/K). Thus, at T > 1000 Heikes formula is not valid for these compounds [15].

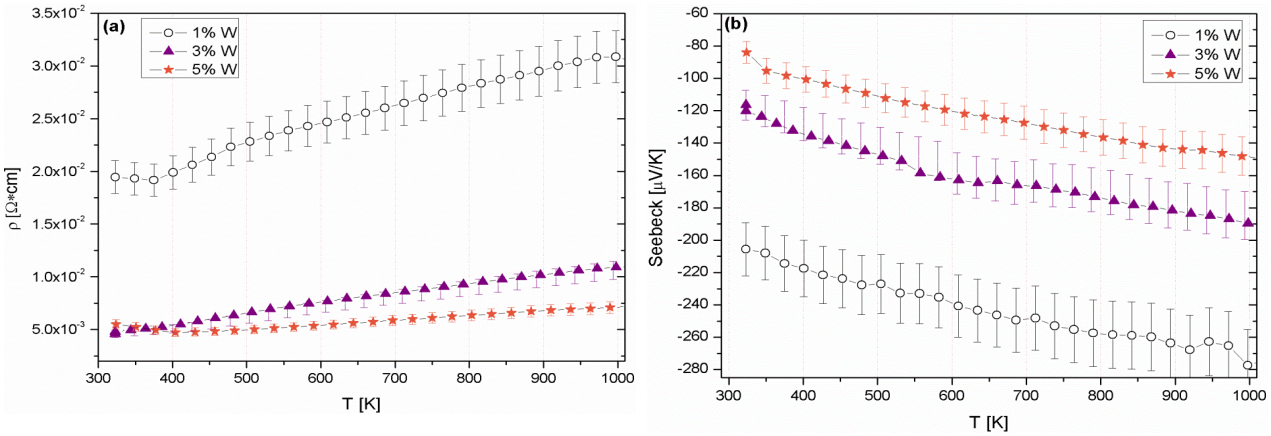

Fig. 19. Temperature dependence of the **a)** resistivity and **b)** Seebeck coefficient of $CaMn_{1-x}W_xO_{3-\delta}$ (x = 0.01; 0.03; 0.05).

The temperature dependence of the thermal conductivity of $CaMn_{1-x}W_xO_{3-\delta}$ (x = 0.01; 0.03; 0.05) is exhibited in Fig.20. The total thermal conductivity of $CaMn_{1-x}W_xO_{3-\delta}$ generally decreases with increasing W substitution. For example, at 400 K $CaMn_{0.99}W_{0.01}O_{3-\delta}$ has a total thermal conductivity of κ_{400} = 2.34 W/m*K while $CaMn_{0.95}W_{0.05}O_{3-\delta}$ has a total thermal conductivity of κ_{400} = 1.97 W/m*K. Due to its higher atomic mass, W atoms provide better phonon scattering in the crystal resulting in a lower thermal conductivity of the compounds.

The total thermal conductivity, κ_{total}, (Fig. 20a) can also be expressed by:

$$\kappa_{total} = \kappa_l + \kappa_e \qquad \textbf{Eq. 5}$$

where κ_l is the lattice contribution and κ_e is the electronic contribution to the total thermal conductivity. The electronic contribution of the thermal conductivity can be approximated from the electrical resistivity data using the Wiedemann-Franz law:

$$\kappa_e = \frac{L_0 T}{\rho} \qquad \textbf{Eq. 6}$$

where L_0 is the Lorenz constant (2.443×10^{-8} WΩ/K) and ρ is the electrical resistivity. κ_e was calculated in this manner in the temperature range of 300 K< T < 1000 K and is plotted in Fig. 20b. κ_e increases with increasing W substitution which is consistent with the rise of the charge carrier concentration. At 800 K for instance, κ_e is 0.069 W/mK; 0.216 W/mK; and 0.307 W/mK for the compounds with 1, 3 and 5 % W substitution, respectively. The percentage of κ_e in the total thermal conductivity κ_{total} is 3.5% (1% W), 10.63% (3% W), and 15.31% (5% W) which is relatively small. Thus, we can conclude that heat conduction in these compounds is predominantly represented by the lattice contribution, κ_l, which was also observed for other substituted $CaMnO_3$ compounds [5, 12, 16, 66]. The values also show that the percentage of κ_e is highest for $CaMnO_3$ with 5% W substitution which also increases the total thermal conductivity of this compound (Fig. 20a).

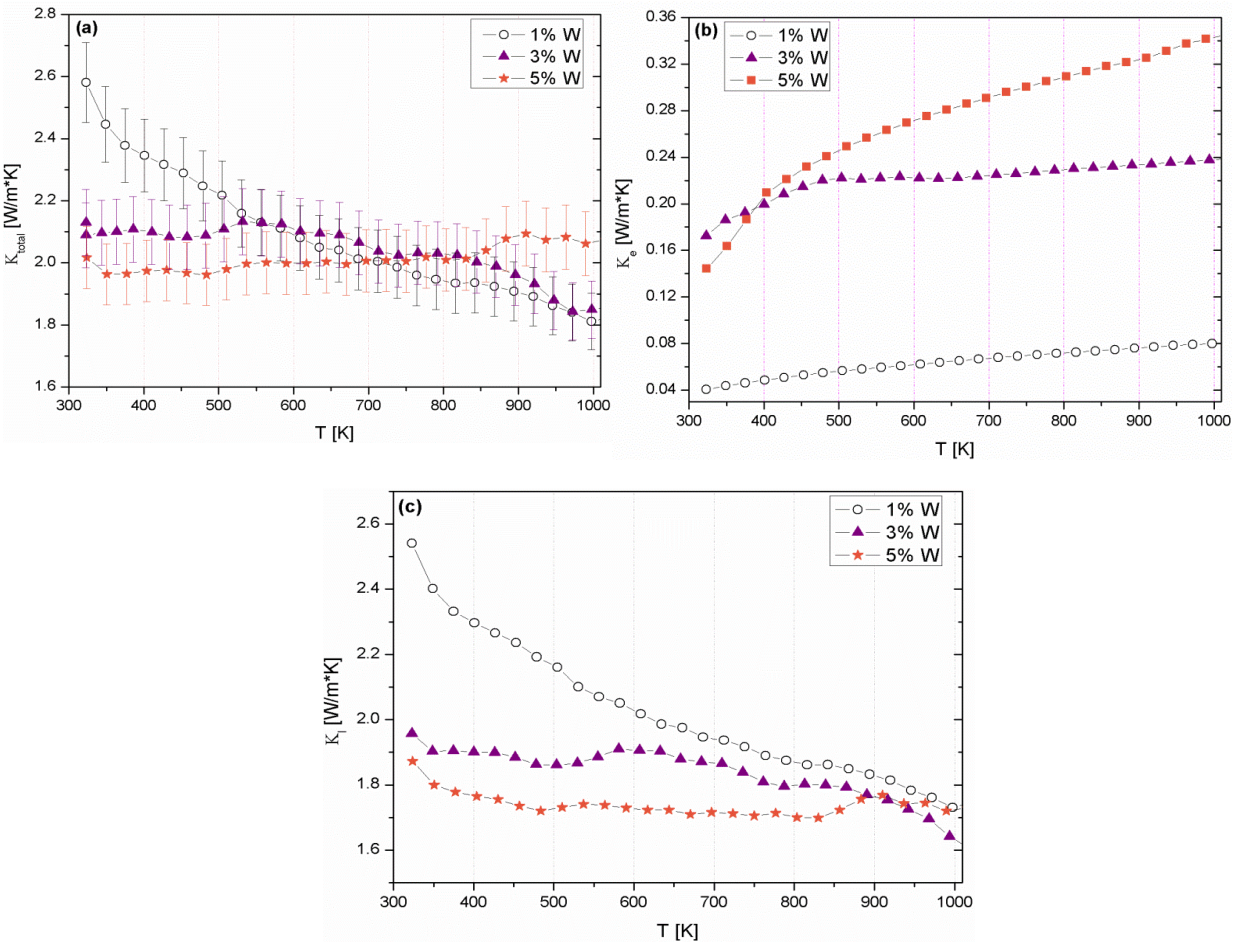

Fig. 20. (a) Total thermal conductivity (κ_{total}); **(b)** electronic thermal conductivity (κ_{el}); **(c)** phonon thermal conductivity (κ_{ph}) of $CaMn_{1-x}W_xO_{3-\delta}$ (x= 0.01; 0.03; 0.05).

The ZT values of the $CaMn_{1-x}W_xO_{3-\delta}$ (x = 0.01; 0.03; 0.05) samples in temperature range of 300 K < T < 1000 K are compared in Fig.21. The highest ZT value is presented by $CaMn_{0.97}W_{0.03}O_{3-\delta}$ (d_{rel} = 84%) with $ZT_{1000\,K}$ = 0.19. This exceeds reported values of other electron doped $CaMnO_3$ compounds by more than 16% [67-71] and can be attributed to the low electrical resistivity (ρ_{1000K} = 0.010 Ωcm) and the low thermal conductivity (κ_{1000K} = 1.84 W/m*K) of $CaMn_{0.97}W_{0.03}O_{3-\delta}$.However, the reported $CaMn_{0.98}Nb_{0.02}O_{3-\delta}$ is still outperforming our compounds with a ZT_{1000K} = 0.32 [15].

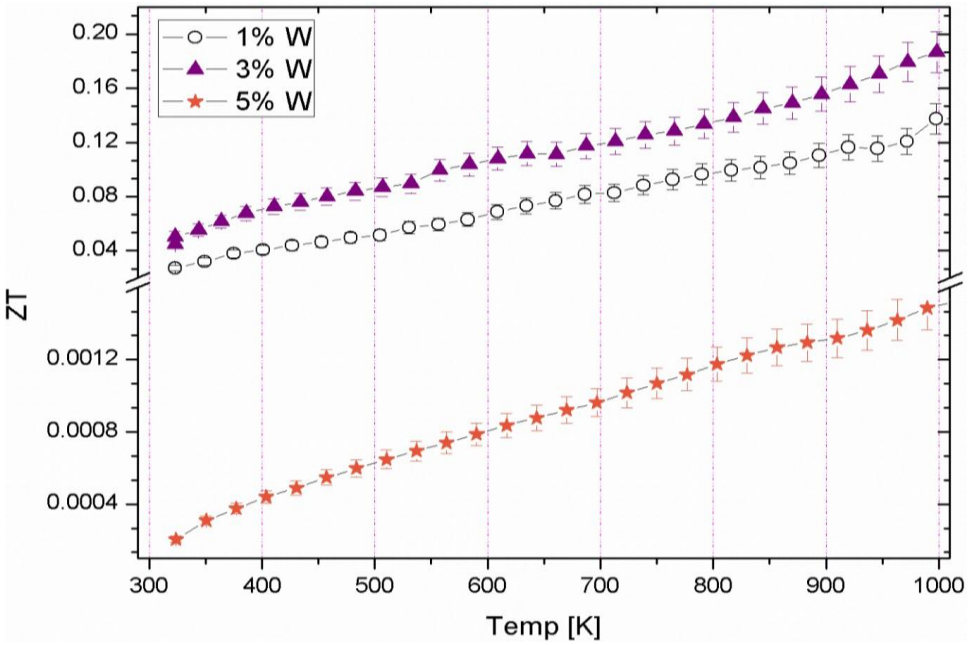

Fig. 21. Temperature dependence of the figure of merit (ZT) of $CaMn_{1-x}W_xO_{3-\delta}$ (x = 0.01; 0.03; 0.05).

5. Conclusion

CaMnO3 is shown to be a promising candidate for thermoelectric application. Its thermoelectric properties can be influenced by element substitutions leading to the creation of Mn^{3+} ions and a hopping mechanism in the resulting Mn^{3+}-O-Mn^{4+} ion network. Moreover, the thermoelectric properties of the $CaMnO_3$ system can be improved by W substitutions, variations of the synthesis method and grain boundary reduction by single crystal growth.

Thin film CaMnO3 shows a high potential for the application in small thermoelectric devices, and it can be further improved by partial substitution of other elements for Ca or Mn. Synthesis using soft chemistry methods has, however, been difficult. Therefore, deposition techniques such as Atomic Layer Deposition (ALD) or Physical Layer Deposition (PLD) are suggested to implement the idea. These methods enable the formation of electron doped $CaMnO_3$ thin films at the nanoscale, which will improve the ZT due to the reduction of the thermal conductivity in low dimensional thermoelectric materials.

6. List of acronyms and symbols

Acronyms

AFM	Antiferromagnetic
DTA	Differential Thermal Analysis
DSC	Differential Scanning Calorimetry
DOS	Density Of States
CA	Citric Acid
EDX	Energy Dispersive X-Ray Spectroscopy
FZ	Floating Zone
LFA	Laser Flash Analysis
LS	Low Spin
PLD	Pulsed Laser Deposition
PM	Paramagnetic
PPMS	Physical Property Measurement System
RP	Ruddlesden-Popper
SEM	Scanning Electron Microscopy
TE	Thermoelectric
TEM	Transmission Electron Microscopy
TGA	Thermogravimetric Analysis
TSFZ	Travelling Solvent Floating Zone
TOM	Thermoelectric Oxide Module
TTO	Thermal Transport Option
VRH	Variable Range Hopping
XRD	X-Ray Diffraction
XRPD	X-Ray Powder Diffraction

Greek symbols

α	Cell parameter
α_d	Thermal diffusivity
γ	Cell parameter
δ	Oxygen nonstoichiometry
κ	Thermal conductivity
κ_{el}	Electronic thermal conductivity
κ_{ph}	Phononic thermal conductivity
ρ	Electrical resistivity
ρ_{rel}	Relative density
σ	Electrical conductivity

Roman symbols

a	Lattice parameter
b	Lattice parameter
c	Lattice parameter
Cp	Heat capacity at constant pressure
d	Relative density of the sample
kB	Boltzmann constant
K	Thermal conductance
L_0	Lorenz number for free electron gas
m	Mass
S	Seebeck coefficient
t	Time
T	Temperature
t_{2g}	Electron occupancy in t_{2g} orbitals
th	Thickness
V	Unit cell volume
V	Voltage
V	Volume
x	Concentration of the substitution
ZT	Figure of Merit

7. References

[1] N. Shutoh, S. Sakurada, *J. Alloys Compd.* 389 (2005) 204-208.

[2] B.C. Sales, D. Mandrus, R.K. Williams, *Science* 272 (1996) 1325-1328.

[3] G.J. Snyder, E.S. Toberer, *Nat Mater* 7 (2008) 105-114.

[4] A. Weidenkaff, L. Bocher, R. Robert, M. Aguirre, D. Logvinovich, *MRS Proceeding* 1044 (2007) 311-317.

[5] Y. Wang, Y. Sui, X. Wang, W. Su, X. Liu, H.J. Fan, *Acta Mater.* 58 (2010) 6306-6316.

[6] S.G. Ebbinghaus, H.-P. Abicht, R. Dronskowski, T. Müller, A. Reller, A. Weidenkaff, *Prog. Solid State Chem.* 37 (2009) 173-205.

[7] R.H. Mitchell, *Perovskites modern and ancient*. Almaz Press, Thunder Bay, Ontario, 2002.

[8] C.N.R. Rao, A.K. Cheetham, R. Mahesh, *Chem. Mater.* 8 (1996) 2421-2432.

[9] B. Raveau, A. Maignan, C. Martin, M. Hervieu, *Chem. Mater.* 10 (1998) 2641-2652.

[10] C.R. Wiebe, J.E. Greedan, J.S. Gardner, Z. Zeng, M. Greenblatt, *Phys. Rev. B: Condens. Matter Mater Phys.* 64 (2001) 644211-644217.

[11] J.A. Souza, J.J. Neumeier, R.K. Bollinger, B. McGuire, C.A.M. dos Santos, H. Terashita, *Phys. Rev. B* 76 (2007) 024407.

[12] A. Maignan, C. Martin, C. Autret, M. Hervieu, B. Raveau, J. Hejtmanek, *J. Mater. Chem.* 12 (2002) 1806-1811.

[13] Y. Zhou, I. Matsubara, R. Funahashi, G. Xu, M. Shikano, *Mater. Res. Bull.* 38 (2003) 341-346.

[14] B. Raveau, C. Martin, A. Maignan, *J. Alloys Compd.* 275-277 (1998) 461-467.

[15] L. Bocher, M.H. Aguirre, D. Logvinovich, A. Shkabko, R. Robert, M. Trottmann, A. Weidenkaff, *Inorg. Chem.* 47 (2008) 8077-8085.

[16] Y. Wang, Y. Sui, H. Fan, X. Wang, Y. Su, W. Su, X. Liu, *Chem. Mater.* 21 (2009) 4653-4660.

[17] D.S. Paik, A.V. Prasada Rao, S. Komarneni, *Journal of Sol-Gel Science and Technology* 10 (1997) 213-220.

[18] L. Bocher, M.H. Aguirre, D. Logvinovich, A. Shkabko, R. Robert, M. Trottmann, A. Weidenkaff, *Inorg. Chem* 47 (2008) 8077-8085.

[19] H.S. Horowitz, J.M. Longo, *Mater. Res. Bull* 13 (1978) 1359-1369.

[20] S.M. Koohpayeh, D. Fort, J.S. Abell, *P. Cryst. Growth. Char. Mater* 54 (2008) 121-137.

[21] P.V. Riboud, A. Muan, *J. Am. Ceram. Soc* 46 (1963) 33-36.

[22] B.D. White, C.A.M. dos Santos, J.A. Souza, K.J. McClellan, J.J. Neumeier, *J. Cryst. Growth* 310 (2008) 3325-3330.

[23] M. Miclau, D. Grebille, C. Martin, *J. Cryst Growth* 285 (2005) 661-669.

[24] J. Rodriguez-Carvajal, *Phys. B: Phys. Condens. Matter.* 192 (1993) 55-69.

[25] J. Laugier, (1996).

[26] G.M. Sheldrick, (1997).

[27] L. Karvonen, S. Yoon, P. Hug, H. Yamauchi, A. Weidenkaff, M. Karppinen, *Mater. Res. Bull.* 46 (2011) 1340-1345.

[28] G.J. Shugar, J.T. Ballinger, L.M. Dawkins, *Chemical technicians' ready reference handbook*. McGraw-Hill, 1996.

[29] L. Karvonen, S. Räsänen, H. Yamauchi, M. Karppinen, *Chem. Lett.* 36 (2007) 1176-1177.

[30] N. Vogel-Schäuble, R. Dujardin, A. Weidenkaff, M. Aguirre, *J. Electron. Mater.* 1-9.

[31] M.E.M. Jorge, A.C. Dos Santos, M.R. Nunes, *International Journal of Inorganic Materials* 3 (2001) 915-921.

[32] H. Taguchi, Y. Kuniyoshi, M. Nagao, *Journal of Materials Science Letters* 10 (1991) 675-676.

[33] C.C.K. Chiang, K.R. Poeppelmeier, *Materials Letters* 12 (1991) 102-108.

[34] R.S. Tichy, J.B. Goodenough, *Solid State Sciences* 4 (2002) 661-664.

[35] D. Flahaut, T. Mihara, R. Funahashi, N. Nabeshima, K. Lee, H. Ohta, K. Koumoto, *Journal of Applied Physics* 100 (2006) 084911.

[36] L. Bocher, M.H. Aguirre, R. Robert, D. Logvinovich, S. Bakardjieva, J. Hejtmanek, A. Weidenkaff, *Acta Mater* 57 (2009) 5667-5680.

[37] D.T.J. Hurle, *Handbook of Crystal Growth*. 1994.

[38] T. Suzuki, H. Sakai, Y. Taguchi, Y. Tokura, *J. Electron. Mater.* 41 (2012) 1559-1563.

[39] D. Prabhakaran, A.I. Coldea, A.T. Boothroyd, S.J. Blundell, *Journal of Crystal Growth* 237-239, Part 1 (2002) 806-809.

[40] K.R. Poeppelmeier, M.E. Leonowicz, J.C. Scanlon, J.M. Longo, W.B. Yelon, *J. Solid State Chem* 45 (1982) 71-79.

[41] B.B. Van Aken, A. Meetsma, Y. Tomioka, Y. Tokura, T.T.M. Palstra, *Physical Review B* 66 (2002) 224414.

[42] A. Reller, J.M. Thomas, D.A. Jefferson, M.K. Uppal, *Proc. R. Soc. Lond. A* 394 (1984) 223-241.

[43] J. Briàtico, B. Alascio, R. Allub, A. Butera, A. Caneiro, M.T. Causa, M. Tovar, *Phys. Rev. B* 53 (1996) 14020.

[44] B. Raveau, Y.M. Zhao, C. Martin, M. Hervieu, A. Maignan, *J. Solid State Chem* 149 (2000) 203-207.

[45] L. Bocher, R. Robert, M.H. Aguirre, S. Malo, S. Hébert, A. Maignan, A. Weidenkaff, *Solid State Sci.* 10 (2008) 496-501.

[46] F. Kawashima, X.Y. Huang, K. Hayashi, Y. Miyazaki, T. Kajitani, *J. Electron. Mater.* 38 (2009) 1159-1162.

[47] S. Urata, R. Funahashi, T. Mihara, A. Kosuga, S. Sodeoka, T. Tanaka, *Int. J. Appl. Ceram. Technol.* 4 (2007) 535-540.

[48] F. Jeffrey W, *J. Eur. Ceram. Soc.* 32 (2012) 525-540.

[49] D. Prabhakaran, A.I. Coldea, A.T. Boothroyd, S.J. Blundell, *J. Cryst. Growth* 237-239 (2002) 806-809.

[50] J.S. Zhou, J.B. Goodenough, *Phys. Rev. B* 66 (2002) 052401.

[51] D.W. Visser, A.P. Ramirez, M.A. Subramanian, *Phys. Rev. Lett.* 78 (1997) 3947-3950.

[52] L. Bocher, M.H. Aguirre, R. Robert, D. Logvinovich, S. Bakardjieva, J. Hejtmanek, A. Weidenkaff, *Acta Mater.* 57 (2009) 5667-5680.

[53] M. Miclau, J. Hejtmanek, R. Retoux, K. Knizek, Z. Jirak, R. Frésard, A. Maignan, S. Hébert, M. Hervieu, C. Martin, *Chem. Mater.* 19 (2007) 4243-4251.

[54] X.Y. Huang, Y. Miyazaki, T. Kajitani, *Solid State Commun.* 145 (2008) 132-136.

[55] L. Bocher, R. Robert, M.H. Aguirre, S. Malo, S. Hébert, A. Maignan, A. Weidenkaff, *Solid State Sci.* 10 (2008) 496-501.

[56] M.H. Aguirre, S. Canulescu, R. Robert, N. Homazava, D. Logvinovich, L. Bocher, T. Lippert, M. Dobeli, A. Weidenkaff, *J. Appl. Phys.* 103 (2008) 013703-6.

[57] D.L. M.H. Aguirre, L. Bocher, R. Robert, S.G. Ebbinghaus and A. Weidenkaff, *Acta Mater.* 57 (2008) 108.

[58] L. Bocher, M.H. Aguirre, R. Robert, D. Logvinovich, S. Bakardjieva, J. Hejtmanek, A. Weidenkaff, *Acta Mater.* 57 (2009) 5667-5680.

[59] K.R. Poeppelmeier, M.E. Leonowicz, J.M. Longo, *J. Solid State Chem* 44 (1982) 89-98.

[60] Z. Zeng, M. Greenblatt, M. Croft, *Phys. Rev. B* 59 (1999) 8784.

[61] C. Zener, *Physical Review* 82 (1951) 403.

[62] L. Pi, S. Zhang, W. Tong, S. Tan, Y. Zhang, *Solid State Commun.* 139 (2006) 460-464.

[63] D.M. Rowe, *Thermoelectrics Handbook - Macro to Nano*. CRC Press/Taylor & Francis Group: Boca Raton, 2006.

[64] F. Kawashima, X.Y. Huang, K. Hayashi, Y. Miyazaki, T. Kajitani, *J. Electron. Mater.* 38 (2009) 1159-1162.

[65] F. Jeffrey W, *J. Eur. Ceram. Soc.* 32 (2012) 525-540.

[66] L. Bocher, M.H. Aguirre, D. Logvinovich, A. Shkabko, R. Robert, M. Trottmann, A. Weidenkaff, *Inorganic Chemistry* 47 (2008) 8077-8085.

[67] R. Funahashi, A. Kosuga, N. Miyasou, E. Takeuchi, S. Urata, K. Lee, H. Ohta, K. Koumoto, International Conference of Thermoelectrics, 2007, pp. 124-128.

[68] A. Kosuga, Y. Isse, Y. Wang, K. Koumoto, R. Funahashi, *Journal of Applied Physics* 105 (2009) 093717.

[69] H. Su, Y. Jiang, X. Lan, X. Liu, H. Zhong, D. Yu, *Phys. Status Solidi A* 208 147-155.

[70] J.W. Park, D.H. Kwak, S.H. Yoon, S.C. Choi, *J. Alloys Compd.* 487 (2009) 550-555.

[71] G. Xu, R. Funahashi, Q. Pu, B. Liu, R. Tao, G. Wang, Z. Ding, *Solid State Ionics* 171 (2004) 147-151.